Solar gas-phase CO_2 hydrogenation by multifunctional UiO-66 photocatalysts

Celia Rueda-Navarro, Zahraa Abou Khalil, Arianna Melillo, Belén Ferrer, Raúl Montero, Asier Longarte, Marco Daturi, Ignacio Vayá, Mohamad El-Roz, Virginia Martínez-Martínez, et al.

Solar gas-phase CO_2 hydrogenation by multifunctional UiO-66 photocatalysts

Celia M. Rueda-Navarro,[1] Zahraa Abou-Khalil,[2] Arianna Melillo,[1] Belén Ferrer,[1] Raúl Montero,[3] Asier Longarte,[4] Marco Daturi, [2] Ignacio Vayá,[1,5] Mohamad El-Roz,[2] Virginia Martínez-Martínez,[4] Herme G. Baldoví,[1,*] Sergio Navalón[1.*]

[1] Departamento de Química, Universitat Politècnica de València, Camino de Vera s/n, Valencia 46022, Spain

[2] - Normandie Université, ENSICAEN, UNICAEN, CNRS, Laboratoire Catalyse et Spectrochimie, 14000 Caen, France.

[3] SGIker Laser Facility, UPV/EHU, Sarriena, s/n, 48940 Leioa, Spain

[4] Facultad de Ciencia y Tecnología, Departamento de Química Física, Universidad del País Vasco (UPV/EHU), Apart. 644, 48080 Bilbao, Spain.

[5] Instituto de Tecnología Química (UPV-CSIC), Universitat Politècnica de València, C/Avenida de los Naranjos s/n, Valencia 46022, Spain

Emails: hergarba@cam.upv.es (H.G.); sernaol@doctor.upv.es (S.N)

Abstract

Solar-assisted CO_2 conversion into fuels and chemical products involves a range of technologies aimed at driving industrial decarbonization methods. In this work we report on the development of a series of multifunctional metal-organic frameworks (MOFs) based on nitro- or amino-functionalized UiO-66(M) (M: Zr or Zr/Ti) supported

RuO_x NPs as photocatalysts, having different energy band level diagrams, for CO_2 hydrogenation under simulated concentrated sunlight irradiation. RuO_x(1wt %; 2.2±0.9 nm)@UiO-66(Zr/Ti)-NO_2 was found to be a reusable photocatalyst and selective for CO_2 methanation (5.03 mmol g^{-1} after 22 h, apparent quantum yield at 350, 400 and 600 nm of 1.67, 0.25 and 0.01%, respectively) and shows about 3-6 times activity compared with previous investigations. The photocatalysts were characterized by advanced spectroscopic techniques like femto- and nanosecond transient absorption, spin electron resonance and photoluminescence spectroscopies together with (photo)electrochemical measurements. The photocatalytic CO_2 methanation mechanism was assessed by operando FT-IR spectroscopy. The results indicate that the most active photocatalyst operates under a dual photochemical and photothermal mechanism. This investigation shows the potential of multifunctional MOFs as photocatalysts for solar-driven CO_2 recycling.

Keywords: heterogeneous photocatalysis; multifunctional metal-organic frameworks: UiO-66 topology; CO_2 methanation; solar light

1. Introduction

The present level of burning fossil fuels to meet the world's energy requirements is steadily raising the CO_2 emissions released into the atmosphere and is responsible for global warming and climate change [1, 2]. There is thus an urgent need to shift from these fuels to renewable energy obtained from natural resources like the sun, wind, water or biomass [3, 4]. The development of technologies based on carbon-free energy carriers like green hydrogen is considered vital to help decarbonize the world's economies [5,6], while carbon capture, storage and utilization (CCSU) are some processes that can minimize the negative effects of CO_2 emissions [7, 8]. Even though certain CCS processes have achieved relative success, most of the technologies used to convert CO_2 into valuable products or fuels are still under development [7-13], including solar-assisted photocatalysis, which is considered to be a promising cost-efficient and sustainable process for recycling CO_2 [14-19]. In 1978 a pioneering study reported on the possibility of reducing CO_2 using GaP as the photocatalyst [20]. Since then, many other inorganic semiconductors[18, 21-24] and more recently perovskites [23, 25], carbon-based materials similar to graphenes[23, 26, 27] or carbon nitrides [23, 28] among others [23, 29] have been used for this purpose. H_2 as the reducing agent seems to be more suitable for achieving better performance than H_2O [30]. Since it is expected that green hydrogen will be economically feasible in the medium- and long-term, this innovation will boost the large scale production of compounds and fuels from CO_2 hydrogenation [31]. Of these, the photocatalytic solar-driven reduction of CO_2 by H_2 to CH_4, a process also termed as the *photocatalytic Sabatier reaction*, is attracting increasing interest for the transition to zero net emissions [32-34]. This process considerably improves the efficiency of the thermo-catalytic reaction even when working under mild reaction conditions [32]. For example, photocatalytic CO_2 methanation can be carried out at much lower reaction temperatures (~ 200 ºC) [25] than the thermo-catalytic version (300-

350 ºC) while achieving similar results [25, 32]. The synthetic methane thus obtained can then be directed to the existing natural gas infrastructures to minimize its implementation costs [33]. In less extent, other important related studies have also shown the possibility of performing the photocatalytic CO_2 [30] or CO [35] hydrogenation into C_{2+} and even C_{5+} value-added chemicals and fuels.

Metal-organic frameworks (MOFs)[36], a relatively new research field for a solar-driven photocatalytic Sabatier reaction, is now under development. MOFs are porous crystalline materials built from multitopic organic ligands coordinated to metal ions, metal clusters or metal-oxo chains [37-39]. For about 20 years MOFs have been considered as highly tunable photocatalysts for many organic and inorganic reactions [31, 40-42]. In the field of CO_2 photoreduction, most of the knowledge achieved so far has come from the liquid-phase reaction using organic solvents in the presence of sacrificial electron donors under UV-Vis or visible light irradiation [40]. Acetonitrile is frequently used as a solvent to favor CO_2 dissolution, while triethanolamine is employed as the electron donor to recover photogenerated holes, minimize electron-hole recombination and thus increase the efficiency of the reduction process [40]. These studies on MOFs represent an interesting area of research in understanding the theoretical and practical aspects of CO_2 conversion.

A series of recent studies have reported on using MOFs as photocatalysts for gas-phase CO_2 reduction by H_2 under interesting reaction conditions for large scale processes. The possibility of using MOF-based materials for the photocatalytic gas-phase Sabatier reaction under UV-Vis at 215 ºC [36] was reported for the first time in 2019. Since then, other studies have described a process with MOF-based photocatalysts modified with RuO_x NPs for solar-assisted CO_2 methanation at 200 ºC. RuO_x NPs are the benchmark co-catalyst in achieving high efficiency during CO_2 (photo)methanation [32]. Some of these photocatalysts include Ti-MOFs, such as MIP-208(Ti) [43] or MIL-125(Ti)-NH_2 [44]

functionalized with NH_2 groups. The presence of amino groups determines the MOF energy band level, i.e. a band gap reduction and a negative shift of the lowest unoccupied crystal orbital (LUCO) with respect to the non-functionalized parent MOF and favors the thermodynamics of the reduction processes [45, 46]. Other studies have reported that amino groups in MOFs favor the stabilization of photogenerated holes and, in turn, the photoinduced charge separation efficiency [47, 48]. Amino-MOFs like UiO-66(Zr)-NH_2 have a higher CO_2 adsorption capacity than the analogous UiO-66(Zr)-NO_2 due to the bonding capacity of the amino groups [49]. Despite the research on the possibility of tuning the energy band diagram of MOFs with functional groups other than amino groups, such as nitro, bromo or methyl groups and their resulting photocatalytic activity, few studies have to date addressed its influence on photocatalytic CO_2 hydrogenation [50,45, 51]. Other related studies have shown that mixed-metal MOFs involve higher photocatalytic activity in CO_2 reduction [45, 52]. For example, the better performance of the UiO-66(Zr/Ti)-based photocatalyst than UiO-66(Zr) is associated with the role of Ti(IV) as the electron mediator that favors photoinduced ligand-to-metal charge transfer (LMCT) processes from the organic ligand to the metal node [52-54]. Despite these important findings, as far as we know, no studies have as yet explored the possibility of developing multifunctional MOF-based materials with a unique energy band diagram determined by the presence of specific functional groups, e.g. the amino or nitro groups, simultaneously containing mixed-metal nodes for more effective photoinduced charge separation and co-catalysts to boost the solar-assisted photocatalytic Sabatier reaction.

In this context, we report here the development of multifunctional nitro- or amino functionalized Zr(IV)- or Zr(IV)/Ti(IV)-based-MOFs with a UiO-66 topology-supported RuO_x NPs for the solar-driven solid-gas phase Sabatier reaction. The materials were characterized by PXRD, analytical, spectroscopic and electron microscopy techniques

and their photocatalytic activities were tested under simulated concentrated sunlight irradiation. Femto- and nanosecond transient absorption (TAS), photoluminescence (PL), electron spin resonance (ESR) and electrochemical impedance (EIS) spectroscopies together with transient photocurrent measurements and additional specific photocatalytic experiments were used to determine the role of MOF counterparts during CO_2 photomethanation via a likely dual photochemical and photochemical mechanism. The photocatalytic CO_2 hydrogenation pathway was studied by operando FT-IR spectroscopy.

2. Experimental section

Details of the materials, preparation, characterization, and photocatalytic procedures used in the study can be found in the Supporting information (S1. Synthesis of the MOF-based materials; S2. Characterization techniques; S3. Photocatalytic activity).

2.1. Materials, preparation methods and characterization.

All the materials employed in this study were of analytical or HPLC grade and supplied by Merck. UiO-66(Zr)-NH_2 and UiO-66(Zr)-NO_2 were prepared according to previous procedures [55-57] and were post-synthetically modified by titanium(IV) chloride tetrahydrofuran complex [$TiCl_4(THF)_2$] complex to obtain UiO-66(Zr/Ti)-NH_2 and UiO-66(Zr/Ti)-NO_2 as reported [58, 59]. RuO_x NPs were supported on these four UiO-66 solids using the photodeposition method [44].

The solids were characterized by powder X-ray diffraction (PXRD), UV-Vis diffuse reflectance (UV-Vis DRS), X-ray photoelectron (XPS), electron spin resonance (ESR), steady-state photoluminescence (PL), electrochemical impedance (EIS), femto- and microsecond transient (TAS) spectroscopies and electron microscopy, including such as transmission electron microscopy (TEM) or scanning transmission electron

microscopy (SEM) coupled with an energy-dispersive X-ray electron (EDX) detector. Isothermal N_2 adsorption, thermogravimetric and photoelectrochemical measurements were also used.

2.3. Photocatalytic activity

Photocatalytic reactions were carried out under batch reaction conditions (S3. Photocatalytic activity) and the data given here are the average of at least three separate experiments.

3. Results and Discussion

3.1. Photocatalyst characterization

The MOF-based materials prepared, i.e. UiO-66(M)-X (M: Zr and/or Ti; X: NH_2 or NO_2), both loaded or unloaded with RuO_x NPs, were characterized by different techniques. PXRD analyses revealed that these solids had the expected UiO-66 topology (Figure 1) [57]. The ICP-OES analyses of acid-digested MOFs were used to quantify the zirconium and/or titanium elements, either loaded or not loaded with RuO_x NPs at 1 wt% of ruthenium. UiO-66(Zr/Ti)-NH_2 and UiO-66(Zr/Ti)-NO_2 have a titanium content of 0.9 and 1.3 wt%, respectively. In this regard, previous studies reported that post-synthetic modification (PSM) of UiO-66(Zr) based materials with $TiCl_4(THF)_2$ complex results in the incorporation of Ti(IV) in the solid by metal exchange and/or grafting onto the metal node at the linker vacancy [60]. Partial replacement of Zr(IV) by Ti(IV) ions with smaller ionic radii contract the unit cell reflected in PXRD by a small negative shift of the position of the diffraction peaks. In the present work, UiO-66(Zr/Ti)-X (X: NH_2 or NO_2) solids showed similar PXRD peak positions to those in zirconium, indicating that Ti(IV) ions are mostly grafted onto the MOF metal nodes [58, 60]. The PXRD of UiO-66 solids loaded with RuO_x NPs have similar features to those of the parent MOFs. The absence of RuO_x

diffraction peaks was attributed to the low ruthenium loading (1 wt%) in the MOF and/or good dispersion of small NPs [44].

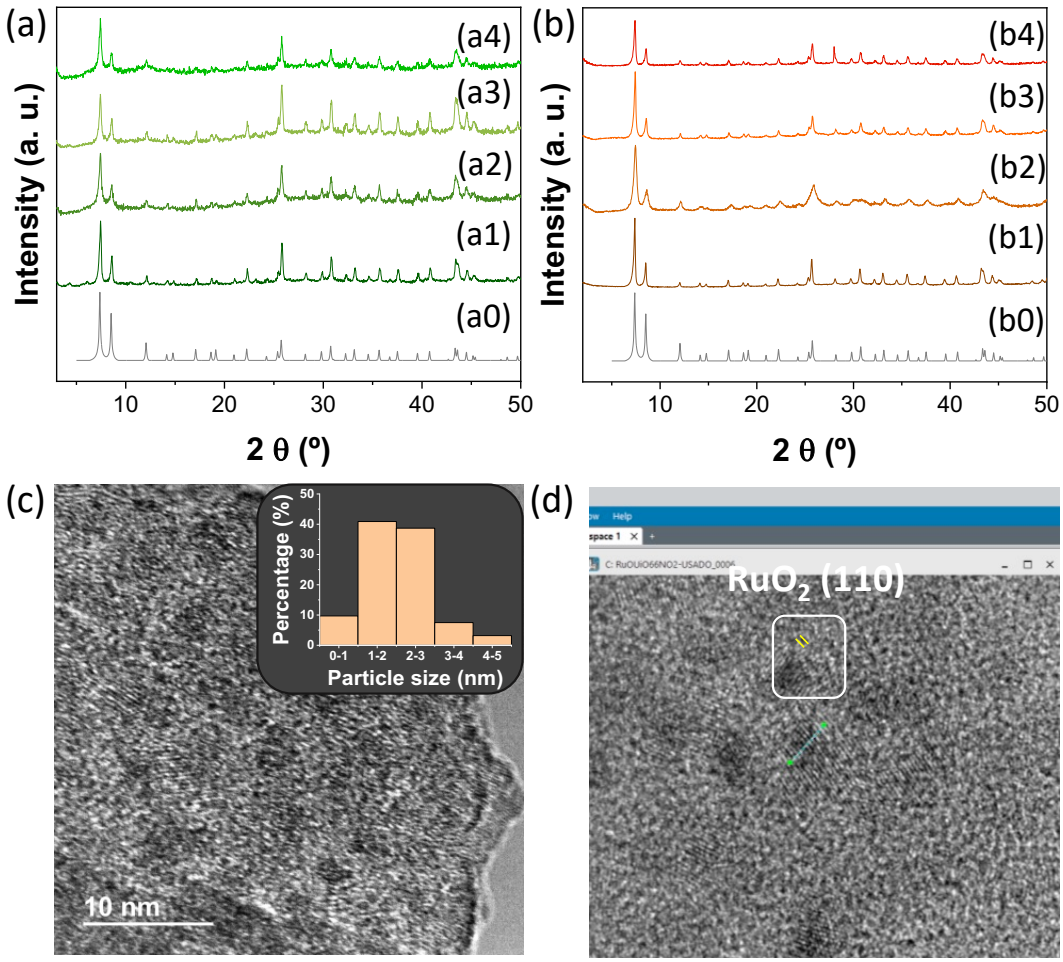

Figure 1. XRD of simulated UiO-66 (a0, b0) or PXRD of UiO-66(Zr)-NH_2 (a) or UiO-66(Zr)-NO_2 (b) materials. Legend panel (a): UiO-66(Zr)-NH_2 (a1), RuO_x@UiO-66(Zr)-NH_2 (a2), UiO-66(Zr/Ti)-NH_2 (a3), RuO_x@UiO-66(Zr/Ti)-NH_2 (a4). Legend panel (b): UiO-66(Zr)-NO_2 (b1), RuO_x@UiO-66(Zr)-NO_2 (b2), UiO-66(Zr/Ti)-NO_2 (b3), RuO_x@UiO-66(Zr/Ti)-NO_2 (b4). (c) HRTEM image and RuO_x particle size distribution of RuO_x@UiO-66(Zr/Ti)-NO_2; RuO_x average particle size and standard deviation of 2.08 ± 0.82 nm. (d) d-spacing determination (0.32 nm) from HRTEM image of RuO_x@UiO-66(Zr/Ti)-NO_2.

The HR-SEM analyses showed that UiO-66 crystals are characterized by the agglomeration of small cubes with average particle sizes and standard deviations of 118 ± 57 nm (Figure S1). HR-SEM in combination with EDX analyses (Figures S2-S10) showed a good distribution of MOF elements within the particles. The relatively low intensity of ruthenium due to its low loading (1 wt% Ru) was within the instrument's detection limit. DF-STEM coupled with EDX and HR-TEM measurements characterized RuO_x NPs (2.14 ± 0.86 nm) supported on UiO-66 particles. HRTEM measurements (Figures S11-S14) indicated the presence of 0.32 nm lattice spacings (Figure S15-S17), characteristic of (110) facet of RuO_2 [61].

The UiO-66 samples were also characterized by XPS (Figure 2 and Figures S18-S21) to determine the oxidation state of the elements within the solids. The XPS spectra of the C 1s region is associated with the presence of the 2-amino or 2-nitroterephthalates ligands of the MOFs: C-C sp^2 bonds (284.4 eV), COO^- groups (288 eV) and C-N bonds of amino or nitro (~285 eV) groups. The N 1s XPS of amino-functionalized UiO-66 solids shows the expected C-N signal at about 399 eV. In the case of nitro-functionalized UiO-66 materials, N 1s XPS spectra are dominated by a main band at 405 eV, due to the nitro group, while a signal associated with the presence of an amino group can also be detected. This situation, i.e. the presence of a small band assigned to the amino group when preparing nitro-functionalized UiO-66 solids, has previously been reported [62]. For the series of RuO_x NPs supported UiO-66 solids, the XPS Ru 3d spectra showed a weak band centered at about 282 eV (Figures S22 and S25), partially overlapping with C-C sp^2 bond signals (284.4 eV), which can be assigned to the presence of RuO_2 NPs [44]. Supported RuO_2 NPs were further characterized by Ru 3p XPS, where the expected two bands could be seen at about 462.5 and 485 eV characteristic of Ru $3p_{3/2}$ and Ru 3 $p_{1/2}$, respectively. The O 1s XPS signal was assigned to the presence of COO^- groups (532 eV) and M-O

bonds (M: Zr, Ti or Ru) (530 eV). Zr 3d and Ti 2p XPS spectra showed the expected signals of Zr(IV) and Ti(IV) ions in the UiO-66 structure. Zr 3d XPS spectra had two bands centered at about 182 and 185 eV due to Zr $3d_{5/2}$ and Zr $3d_{3/2}$, respectively. The XPS spectra of the Ti 2p region for mixed-metal UiO-66(Zr/Ti)-X (X: NH_2 or NO_2) confirmed the presence of Ti(IV) indicated by two bands at 459 and 464 eV due to Ti $2p_{3/2}$ and Ti $2p_{1/2}$, respectively.

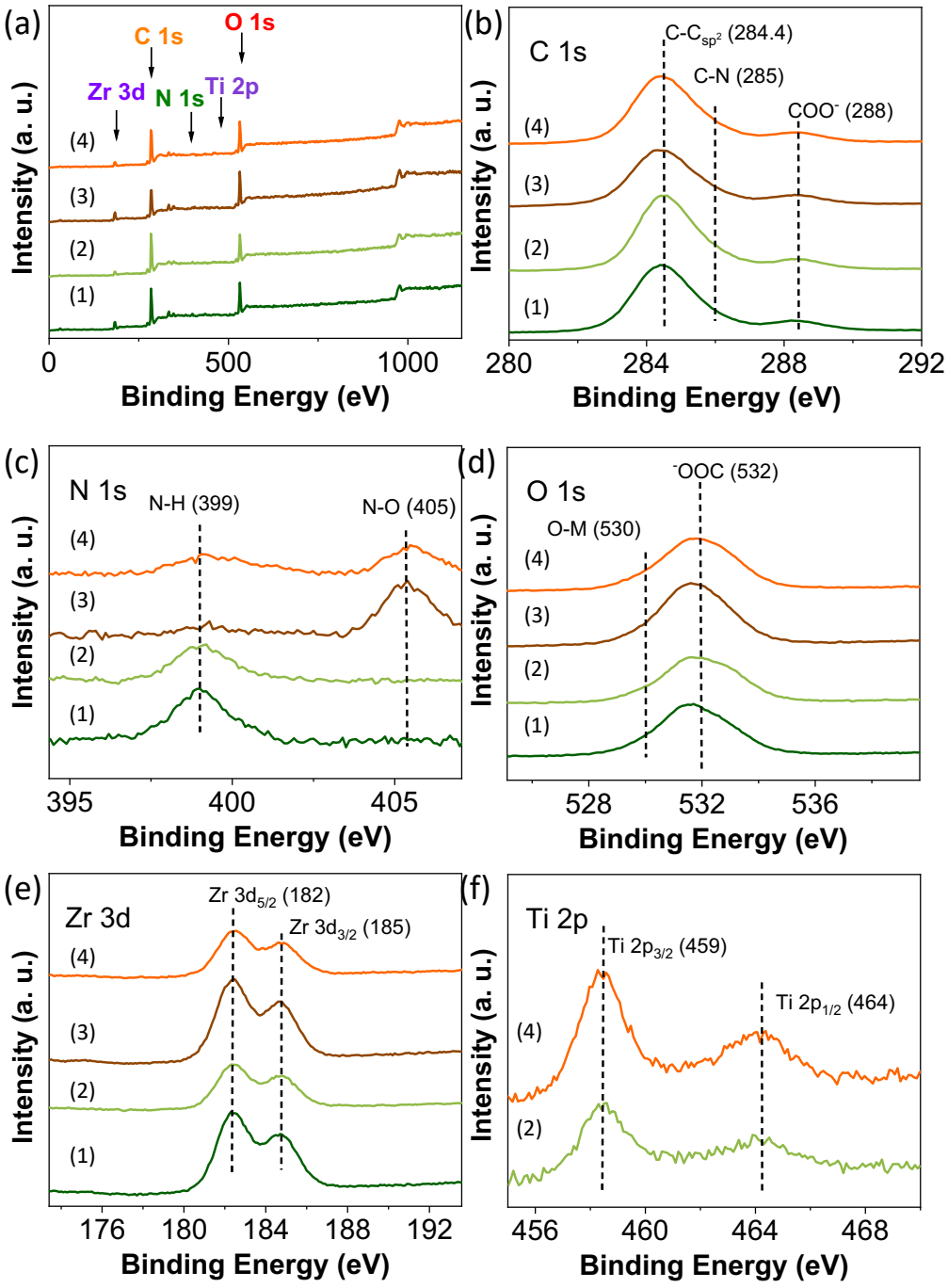

Figure 2. XPS survey (a), C 1s (b), O 1s (c), N 1s (d), Zr 3d (e) and Ti 3p (f) of UiO-66(Zr)-NH_2 (1), UiO-66(Zr/Ti)-NH_2 (2), UiO-66(Zr)-NO_2 (3), UiO-66(Zr/Ti)-NO_2 (4).

The UiO-66 solids were analyzed by FT-IR spectroscopy (Figure S26). In all cases, COO^- groups were characterized by stretching vibrations at about 1574 and 1423

cm^{-1}, respectively. Amino-functionalized UiO-66 solids showed two bands at 3488 and 3374 cm^{-1} due to the asymmetric and symmetric vibrations of $-NH_2$, respectively, together with another band at 1255 cm^{-1} due to C-N stretching vibration. In the case of nitro-functionalized UiO-66 solids, two bands could be seen at about 1543 and 1496 cm^{-1} due to the characteristic asymmetric and symmetric vibration bands of this group, respectively. These spectra also showed small bands attributable to the presence of amino groups, in good agreement with the XPS analyses. These XPS and FT-IR results indicate a need for the development of new synthetic methodologies to prepare UiO-66 solids with only 2-nitroterephthalte ligands in their structure.

Isothermal N_2 adsorption measurements were used to estimate the BET surface areas (Figure S27) and pore volumes of pristine mono- and bimetallic UiO-66 solids with values ranging from 600 to 700 m^2/g and 0.23 to 0.26 cm^3/g, respectively, in agreement with previous studies [58]. TGA analyses under oxidant (air) or inter (nitrogen) atmospheres further confirmed that these UiO-66 samples were thermally stable at temperatures of about 300 ºC in agreement with previous reports (Figure S28) [58, 63, 64]. It should be commented that the stability observed below 300 ºC under these atmospheres might differ somehow the stability under the reaction conditions of photocatalytic CO_2 hydrogenation (H_2:CO_2 molar ratio 4:1 at 200 ºC). Additionally, a control experiment revealed that the TGA of the most active UiO-66(Zr/Ti)-NO_2 solid previously submitted to these reaction conditions exhibited a very similar TGA profile under air than the fresh sample and, thus, confirming its relatively stability under studied reaction conditions.

The optical properties of the UiO-66 materials were studied by UV-Vis DRS measurements. Figure 3 shows that the presence of NO_2, and especially NH_2, groups in the MOF organic ligand favors visible light absorption with absorption onsets at about 400 and 450 nm, respectively. In the case of amino-functionalized UiO-66 solids the band

centred about 365 nm is due to the interaction of the lone pair of electrons (n) of amino group with the π^*-orbital of aromatic ring and this situation results in a new higher HOCO level that favours visible light absorption [65]. Tauc plot analyses using the UV-Vis DRS data (Figure S29) confirmed that the optical band gaps of amino-functionalized UiO-66 solids were lower than the nitro-functionalized UiO-66 solids [66]. Besides, mixed-metal UiO-66 solids exhibit somehow lower optical band gaps associated with the role of Ti(IV) ions as electron mediators in agreement with previous experimental [48, 59] and theoretical studies [67]. XPS valence band measurements (Figure S30) were used to estimate the UiO-66 energy band diagrams together with the optical band gaps. In general, all the solids possessed the thermodynamic requirements for photocatalytic CO_2 hydrogenation under sunlight irradiation, while the UV-Vis DRS of RuO_x NPs on UiO-66 solids showed an extra weak absorption band in the visible region associated with the resonance plasmon band of these NPs (Figure S31).

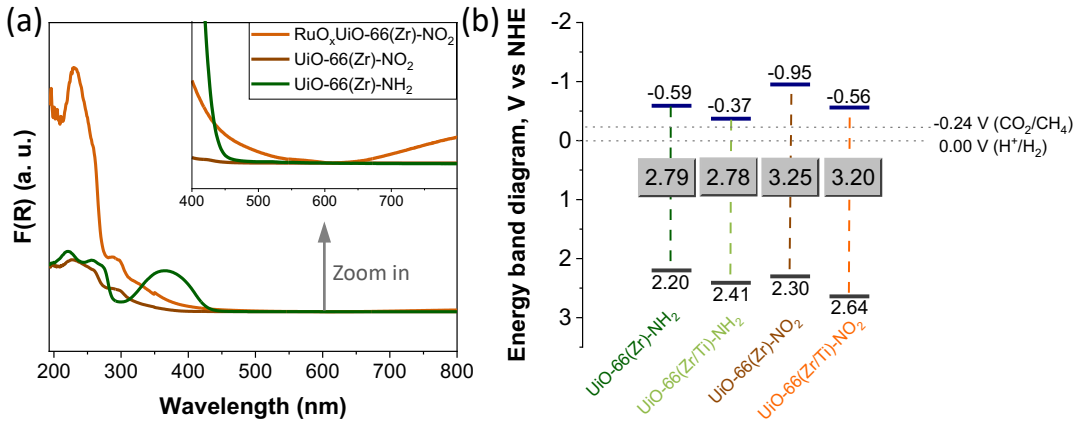

Figure 3. (a) UV-Vis DRS and (b) energy band level diagram of UiO-66 solids as indicated.

3.2. Photocatalytic CO_2 hydrogenation

UiO-66-based solids were first tested as photocatalysts for CO_2 hydrogenation at 200 ºC under simulated concentrated sunlight irradiation (200 mW/cm^2). For this purpose, the quart reactor is heated with a mantle , then, the system irradiated (see details in experimental section). It should be remembered that one sun is defined as 100 mW/cm^2 of irradiance. From the point of view of practical applications, solar concentrators could be used to reach the simulated concentrated sunlight irradiations used in this study. Pristine UiO-66 solids showed little activity and methane was the only product detected (< 30 μmol g^{-1}). Specifically, to illustrate the importance of supported RuO_x NPs in enhancing the activity the performance of UiO-66(Zr)-NH_2, UiO-66(Zr/Ti)-NH_2, UiO-66(Zr)-NO_2 and UiO-66(Zr/Ti)-NO_2 their photocatalytic activities were carried out and the results indicate a production of only 2, 13, 3 and 4, respectively. However, RuO_x NPs supported UiO-66 materials boosted activities toward methane generation by various degrees, in agreement with the role of RuO_x NPs as benchmark co-catalyst for selective CO_2 (photo)catalytic methanation [32]. RuO_x NPs have the ability to favor chemisorption CO_2 and its reaction intermediates like CO or H_2CO with sufficient strength to be completely hydrogenated to methane [34]. Even though our analyses allow identification and quantification of several carbon products such as CO or short-chain hydrocarbons (see supporting information section S3.), methane was the only product detected for all tested photocatalysts (cross-check selectivity with Caen). In other words, all (photo)catalytic tests carried out in this study resulted in methane selectivities higher than 99.8 % (cross-check with Caen) 98.1 %.Control experiments in which CO_2 was replaced by Ar did not indicate the formation of methane or any other product. Due to the similar particle size distribution of RuO_x NPs supported on UiO-66 solids, i.e. a mean average particle size and standard deviations of 2.14 ± 0.04 nm, we consider that the composition

of the UiO-66 photocatalysts determines the resulting activities. Furthermore, it was found that product selectivity is not influenced by the use of UiO-66 composition loaded or not with RuO_x NPs. As an example, the product selectivity distribution of the most active RuOx@UiO-66(Zr/Ti)-NO_2 indicates a CH_4 selectivity higher than 99.8 % (cross-check with Caen). Figure 4 shows that nitro-functionalized UiO-66 photocatalysts are more active than amino-functionalized UiO-66 photocatalysts. This is an important finding since, as commented in the introduction's section, amino-functionalized MOFs like UiO-66 are among the preferred solids for photocatalytic applications, including CO_2 reduction. Regardless of UiO-66(Zr)-NO_2's higher optical band gap than UiO-66(Zr)-NH_2 (3.16 vs 2.79 eV), its better reduction and oxidation capacity than those of the amino group seems to determine its photocatalytic activity (see Figure 3). Figure 4 also shows that the photocatalytic activities of RuO_x NPs supported UiO-66(Zr)-X (X: NH_2 or NO_2) are further increased by the preparation of analogous mixed-metal Zr/Ti materials. Previous studies have demonstrated the role of Ti(IV) ions in the metal node of UiO-66(Zr/Ti)-NH_2 as photoinduced electron transfer mediators [48, 59]. As will be shown below, the better performance of mixed-metal UiO-66 photocatalysts supported by RuO_x NPs than those analogous monometallic ones, can be attributed to increased photoinduced charge separation efficiency, as shown by the spectroscopic and electrochemical characterization.

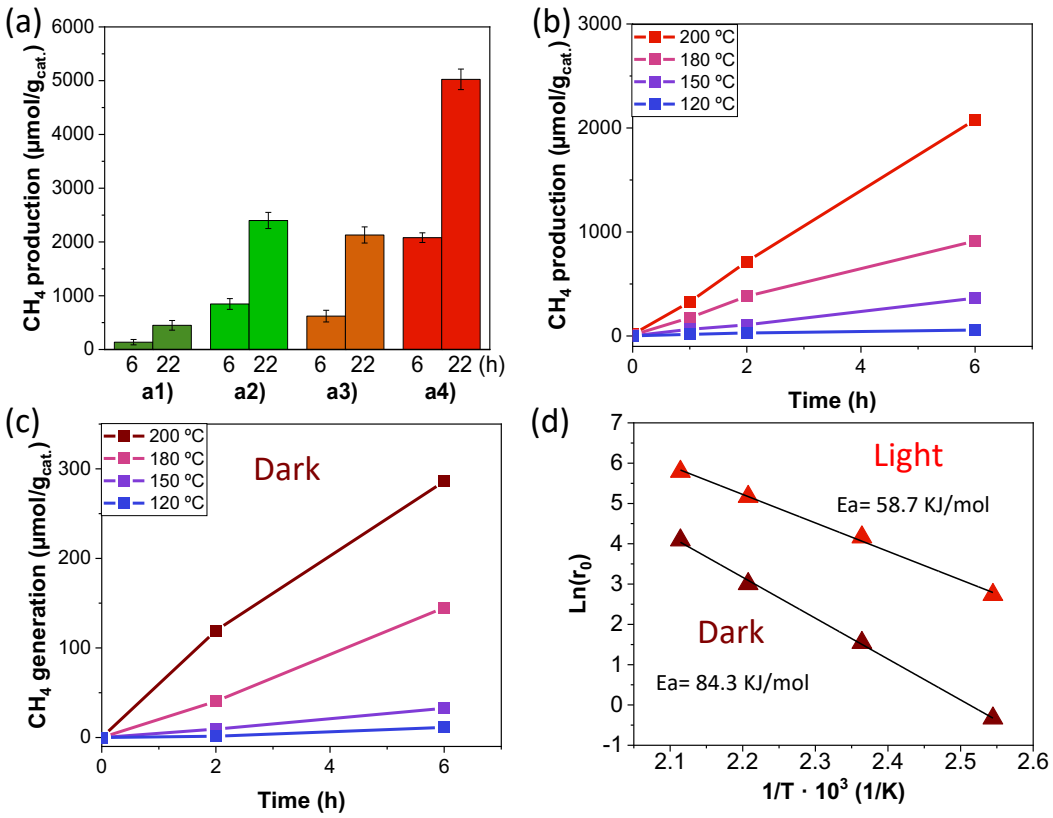

Figure 4. (a) Photocatalytic CO_2 methanation using RuO_x@UiO-66 solids under simulated concentrated sunlight irradiation. Legend: (a1) UiO-66(Zr)-NH_2, (a2) UiO-66(Zr/Ti)-NH_2, (a3) UiO-66(Zr)-NO_2, (a4) UiO-66(Zr/Ti)-NO_2. Influence of reaction temperature on methane generation during photocatalytic CO_2 reduction in light (b) or dark (c) conditions. (d)The Arrhenius plot obtained from initial reaction rates of methane generation as a function of the reaction temperature. Reaction conditions: photocatalyst (15 mg), CO_2:H_2 (1:4), 200 ºC, simulated concentrated sunlight (200 mW/cm^2) irradiation.

To further verify the role of nitro or amino groups in UiO-66(Zr)-X (X: NO_2 or NH_2) on the resulting photocatalytic activity, an analogous photocatalyst termed as UiO-66(Zr) was prepared using terephthalic acid as organic ligand and further modified with RuO_x NPs by photodeposition method. The samples were characterized by PXRD,

spectroscopic (UV-Vis, XPS), analytical (TGA), textural (isothermal N_2 adsorption) and electron microscopic techniques (Figures S32-S37). PXRD confirmed that RuO_x@UiO-66(Zr) and UiO-66(Zr) samples are isostructural crystalline materials with UiO-66 topology (Figure S32). XPS analyses revealed the general expected features of XPS C 1s, O 1s, Zr Ru 3d and 3p (FigureS33). These solids are constituted by particles of 98 ± 63 nm nm as revealed by SEM analyses(FigureS34). TEM measurements revealed the presence of supported RuOx NPs with sizes of 2.4 ± 0.8 nm (FigureS35). The sample exhibited good porosity (1008 m^2/g and 0.38 cm^3/g) and thermal stability under air atmosphere (> 400 ºC) (FigureS36). The energy band level diagram of UiO-66(Zr) is characterized by a wide optical band gap (3.7 eV) with HOCO and LUCO positions of +1.81 and -2.15 V, respectively. The use of RuO_x@UiO-66(Zr) and pristine UiO-66(Zr) as photocatalysts under conditions described in Figure 4 showed a selective methane production of of respectively 500 and 2 μmol g^{-1} after 22 h. The activity of this RuO_x@UiO-66(Zr) photocatalyst is slightly lower to that of RuOx@UiO-66(Zr)-NH_2 and about three times lower than that achieved using RuOx@UiO-66(Zr)-NO_2 photocatalyst. Regardless the lower CO_2 adsorption capacity and higher optical band gap of UiO-66(Zr) compared to UiO-66(Zr)-NH_2 their photocatalytic activities are similar to each other. In contrast, as previously commented RuO_x@UiO-66(Zr)-NO_2 exhibits the higher activity and associated to its unique structure due to the presence of nitro functional groups.The performance of the most active RuO_x@UiO-66(Zr/Ti)-NO_2 sample (~13% CO_2 conversion; 5.03 $mmol_{CH4}\cdot g^{-1}$ after 22 h) during photocatalytic CO_2 hydrogenation to CH_4 was further studied. A photocatalytic experiment using labelled $^{13}CO_2$ and gas-phase aliquot analysis by GC coupled to mass spectrometry confirmed the formation of $^{13}CH_4$ (m/z 17) after 22 h of reaction at 200 ºC (Figure S38). A control experiment under dark reaction conditions at 200 ºC also revealed lower CH_4 production (1.9 mmol g^{-1} after 22

h) than that achieved under simulated concentrated sunlight irradiation. The observation of some activity under dark reaction conditions was not unexpected, since previous studies have reported that RuO_x NPs are an active and selective co-catalyst during thermal catalytic processes [32]. Quantitative information on the performance of RuO_x@UiO-66(Zr/Ti)-NO_2 as photocatalyst at 200 ºC was obtained by estimating the apparent quantum yield (AQY) at specific wavelengths. After deducting the activity observed under dark reaction conditions, the AQYs achieved by irradiation at 350, 400 and 600 nm were 1.67, 0.25 and 0.01, respectively. The influence of the reaction temperature on the photocatalytic activity of RuO_x@UiO-66(Zr/Ti)-NO_2 was then studied (see results in Figure 4b). As can be seen, photocatalytic methane generation as a function of the reaction temperature follows the Arrhenius law and allowed us to estimate an apparent activation energy (Ea) of 58.7 kJ/mol. In a series of analogous experiments carried out in the absence of irradiation (thermal catalysis), the estimated Ea resulted to be 90 kJ/mol. Based on analogous studies [68-70] and as it will be further studied in section 3.3, this significant decrease in Ea can be attributed to the operation of a photothermal reaction pathway.

The photocatalytic activity of RuO_x@UiO-66(Zr/Ti)-NO_2 was compared with those MOF-based photocatalysts reported in previous studies and the results are summarized in Table S1. RuO_x NPs supported trimetallic UiO-66(Zr/Ce/Ti) was recently reported as one of the most active MOF-based photocatalysts for CO_2 methanation under simulated concentrated sunlight irradiation (1.8 mmol g^{-1} CH_4 after 22 h at 200 ºC) (Table S1, entry 2), showing that the activity of RuO_x@UiO-66(Zr/Ti)-NO_2 is about 3 times higher than this photocatalyst under similar reaction conditions. Furthermore, RuO_x@UiO-66(Zr/Ti)-NO_2 exhibits an activity 3-6 times higher than that achieved using analogous solids based on RuO_x NPs supported on Ti-based MOFs, such as MIL-125(Ti)-NH_2 (Table S1, entries 3 and 4) or MIP-208(Ti) (Table S1, entry 5). It is remarkable that the activity of

RuO_x@UiO-66(Zr/Ti)-NO_2 (Table S1, entry 1) is more than two times compared with RuO_x@MIL-125(Ti)-NH_2 (Table S1, entry 4) having the doble amount of ruthenium (2 wt%). It should be noted that all these photocatalysts have a similar RuO_x NP loading (1 wt % of ruthenium) and an average particle size (~ 2 nm). The higher activity of RuO_x@UiO-66(Zr/Ti)-NO_2 thus appears to be related to the energy band diagram level of the photocatalyst determined by the combination of 2-nitroterephthalates ligands and mixed-metal Zr(IV)/Ti(IV) metal nodes, which boosts the efficiency of the reaction. Regardless of these comments, it is pertinent to mention that the state-of-the-art in current photocatalytic gaseous methanation has reported activities, in some cases, greater than 100 mmol g^{-1} h^{-1}. In one of these examples, a ultrathin Mg-Al layered double hydroxide nanosheet supported Ru NPs was found to achieve efficient photothermal CO_2 methanation (277 mmol h^{-1} g^{-1}; 300 W Xe lamp) under continuous flow operation [71].

The activity and stability of RuO_x@UiO-66(Zr/Ti)-NO_2 were studied by performing consecutive reuse experiments. Figure 5 shows that the photocatalyst can be reused without significant loss of activity for four consecutive times with an accumulated reaction time of 90 h. According to PXRD analysis, the crystallinity of the four-times used photocatalyst is preserved. TEM analyses of the reused photocatalyst confirmed that RuO_x average particle size and standard deviation (2.32 ± 0.90 nm) are similar compared to the fresh sample (2.08 ± 0.82 nm). Besides, HR-TEM characterization of the used photocatalyst revealed the presence of lattice fringes with spacings of about 0.203 and 0.32 nm, which were ascribed to the crystal planes (101) and (110) of Ru(0) and RuO_2, respectively (Figure S39).

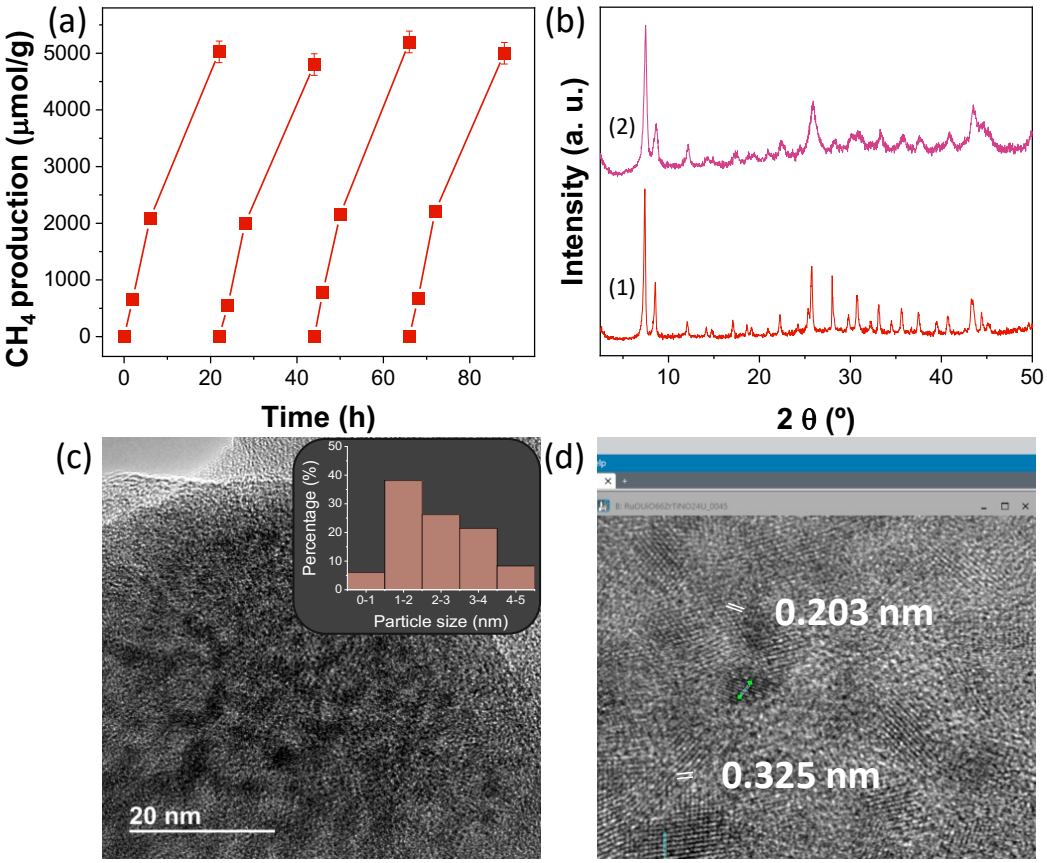

Figure 5. (a) Reusability of RuO_x@UiO-66(Zr/Ti)-NO_2 during photocatalytic CO_2 methanation. (b) PXRD of RuO_x@UiO-66(Zr/Ti)-NO_2 fresh (1) and used (2). (c) TEM image and particle size distribution of used photocatalyst; (d) HRTEM for interplanar distance.

C 1s, O 1s, Zr 3d and Ti 2p XPS analyses of the four-times used photocatalyst (Figure S40) showed similar features to those of the fresh material, while N 1s and Ru 3d XPS showed small but appreciable differences with respect to the fresh sample (Figure 6 and S41). N 1s XPS of the used photocatalyst revealed slight hydrogenation of the nitro group to the amino group (Figure 5). Specifically, the fresh and used RuO_x@UiO-66(Zr/Ti)-NO_2 photocatalysts have a proportion in weight percent of NO_2 versus NH_2 of 55.2/44.8 and 46.8/53.2, respectively. Although partial reduction of NO_2 to NH_2 is

observed in the used RuO_x@UiO-66(Zr/Ti)-NO_2 photocatalyst by XPS, the structural integrity of the used photocatalyst still contains enough NO_2 groups (46.8 at%) to promote the photocatalyst activity without much significant difference (Figure 6). Furthermore, UV-Vis DRS of the used sample showed an extra absorption band with onset absorption at about 430 nm, which agrees with partial nitro hydrogenation to the amino group (Figure 5). In the case of Ru 3d XPS, a small shift of the Ru 3 $d_{5/2}$ was seen toward lower binding energies with respect to the fresh sample (281.9 vs 280.8 eV). These results agree with previous studies that also showed the supported RuO_x NPs employed as co-catalysts during (photo)catalytic hydrogenations at temperatures of about 200 ºC can be converted in some extent to metallic phase [44, 71-74].

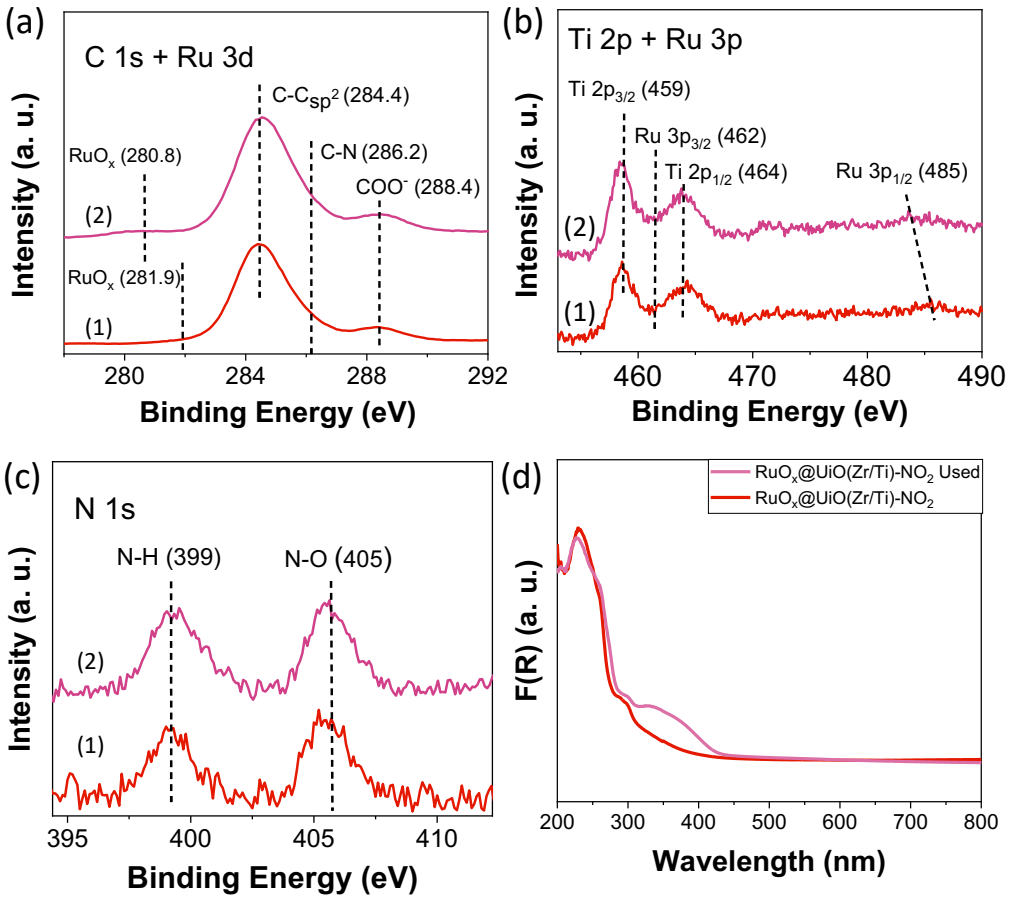

Figure 6. (a) C1s + Ru 3d, (b) Ti 2p + Ru 3p, (c) N 1s XPS of fresh (1) and used (2) photocatalyst and (d) UV-Vis of fresh and used RuO_x@UiO-66(Zr/Ti)-NO_2,

In the present study, additional *in situ* XPS experiments where the fresh RuO_x@UiO-66(Zr/Ti)-NO_2 sample is submitted to a H_2 thermal treatment at 200 ºC also revealed that supported RuO_x NPs are susceptible to be partially reduced to metallic NPs under the studied reaction conditions (Figure S42). It should be noted that metallic ruthenium species have been proposed as responsible species to activate molecular H_2 and initiate CO_2 hydrogenation. [71, 72, 74, 75] Besides, as it will be shown latter RuO_x and Ru species also favor CO_2 and CO chemisorption as evidenced by FT-IR spectroscopy. Overall, these results demonstrate that RuO_x NPs supported on UiO-66(Zr/Ti)-NO_2 are partially reduced during the photocatalytic CO_2 hydrogenation process leading to co-existence of supported RuOx and Ru(0) species within the photocatalyst.

In the area of photocatalysis using MOFs, some studies have reported UV-Vis irradiation of carboxylate-based MOFs at 200 ºC that resulted in partial decarboxylation [76]. To address this issue, a photocatalytic control experiment in which CO_2 was replaced by Ar revealed the presence of CO_2, attributed to the partial decarboxylation of the terephthalate MOF ligand during the reaction (1.8 wt% respect to the amount of the initial carboxylate). These results indicate a need to develop active MOF-based photocatalysts that can operate under milder reaction conditions where their operational stabilities. where their operational stabilities.

3.3. Photocatalytic reaction pathways

3.3.1. Exploration of photochemical and photothermal reaction mechanisms

Based on previous reports, photocatalytic CO_2 reduction using metal/metal oxide NPs supported on MOFs or other materials can occur via a photochemical [24, 34] and/or photothermal reaction mechanisms [24, 34, 77-79]. During the photochemical pathway, the irradiation of the photocatalysts results in the formation of reducing and oxidizing electron and hole pairs, respectively. This is a common reaction mechanism found when using MOFs as photocatalysts, when their irradiation by appropriate wavelengths produces photoinduced electron transfer from the organic ligand to the metal node [43]. The presence of MNPs like RuO_x as co-catalysts can also favor photochemical pathway efficiency by opening new channels for charge carrier separation and enhancing photocatalytic activity [44]. RuO_x NPs have also been reported to promote the photothermal reaction pathway in which light energy is transformed into heat, which favors CO_2 methanation [77].

Several characterization techniques were used to further study these possible reaction pathways using RuO_x NPs supported UiO-66(Zr and/or Ti)-X (X: NH_2 or NO_2). It should be noted that, as shown in Figure 6, the RuO_x@UiO-66(Zr/Ti)-NO_2 photocatalyst used exhibits a partial reduction of supported RuO_x NPs with respect to the fresh sample. To consider the possible influence of the RuO_x oxidation state on the subsequent characterization data, some comparative measurements were carried out using both fresh and used photocatalysts.

To evaluate the photoinduced processes arising from excitation of the different UiO-66(Zr/Ti)-X (X: NH_2 or NO_2) photocatalysts at 267 nm[30, 77] were first studied by femtosecond transient absorption spectroscopy (fs-TAS). This technique has been shown

to be sensitive and precise for investigating processes occurring at a very early stage after excitation, including ultrafast electron transfer or charge separation [80]. The recorded transient absorption spectra (Figure S43) and kinetics (Figures S344) of UiO-66(Zr)–NH_2 showed good agreement with previously reported observations [81], while notable differences were found in the transient absorption spectra when using NO_2 (Figures S45). Transient absorbance of the latter samples covers the entire visible spectrum and does not exhibit any remarkable band/feature (Figures S45). A set of the kinetic traces ranging from 550 to 750 nm were analyzed by means of a global fit, including two-time constants, to describe the dynamics during the first ns after photoexcitation. Table S2 includes the resulting time constants for all the species studied. The fastest components (of the order of a few tens of ps) were associated with electron transfer processes from HOCO to LUCO of MOFs [81], while the longer-lived components, which remained up to the nanosecond time scale, were assigned to a deep trap state [82]. Figures 7a shows for nitro-functionalized UiO-66 solids a comparison of the transients together with the average lifetimes calculated for each probe wavelength on the basis of the time constants derived from the global fit. The data reveal that the fastest relaxation dynamics are those of RuO_x@UiO-66(Zr/Ti)-NO_2, followed by an analogous mixed-metal UiO-66(Zr/Ti)-NO_2 parent sample, while monometallic UiO-66(Zr)-NO_2 exhibited longer-lived components. Similar conclusions can be drawn for amino-functionalized UiO-66 materials (Figure S44). In this regard, kinetic traces have been used as indicators to evaluate electron-hole separation efficiency of the photocatalysts. It is therefore proposed, by means of comparisons with previous ultrafast results from related MOFs,[81] that the faster the relaxation dynamics, the higher the charge-separation efficiency. In fact, the order of photocatalytic activity in our case agrees, to some extent, with the relaxation trace kinetics using ultrafast TAS measurements.

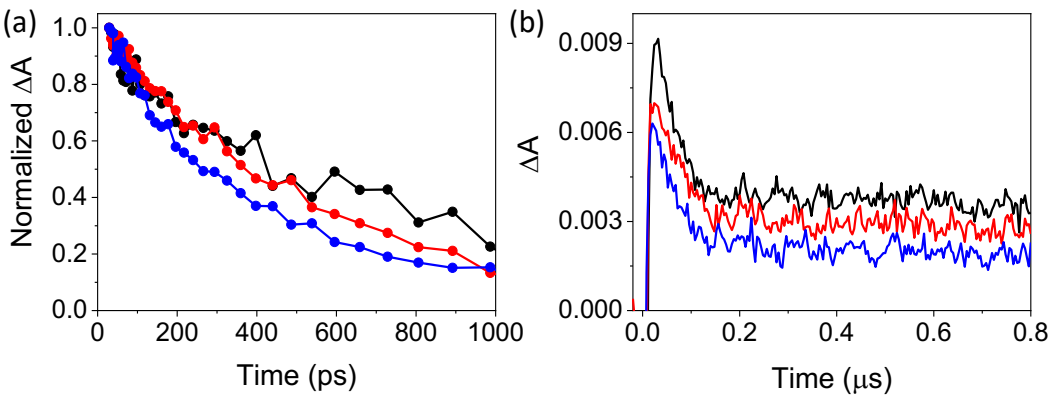

Figure 7. (a) Femtosecond transient absorption recorded at 586 nm and (b) LFP decay traces recorded at 520 nm for UiO-66(Zr)-NO_2 (black), UiO-66(Zr/Ti)-NO_2 (red) and RuO_xUiO-66(Zr/Ti)-NO_2 (blue). FTA measurements were performed at λ_{exc} = 267 nm in aerated MeCN, whereas those of LFP were done at λ_{exc} = 266 nm in MeCN under Ar atmosphere.

Long-lived trap states for UiO-66 photocatalysts were further investigated on longer timescales by the laser flash photolysis (LFP) technique at λ_{exc} = 266 nm. The spectra obtained for the different nitro- (Figures 7b and S46) and amino- (Figures S47), functionalized UiO-66 photocatalysts in an Ar atmosphere on the nanosecond timescale and characterized by a continuous absorption band from 300 to 750 nm. Previous TAS studies by some of us using UiO-66(Zr)-X (X: NH_2 or NO_2) assigned these transient absorption bands to photogenerated electron and holes based on selective quenching experiments [50, 55]. Similar conclusions have been obtained in the present case using methanol as hole quencher for the series of amino-functionalized UiO-66 solids. Figure S48 shows that methanol quenches the region from 300 to 400 nm, resulting in a parallel increase of the transient signals around 600 nm, which indicates that hole deactivation enhances the yield of photogenerated electrons, an effect previously found in other related MOF-based photocatalysts [83, 84]. These results agree with those obtained from ultrafast

TAS and demonstrate the photogeneration of charge separation species as electrons and holes. In line with the ultrafast results, LFP decay traces at 400 and 680 nm show that the faster the decay components (see Table S2), the higher the photocatalytic activity of all the studied RuO_x NPs supported UiO-66(Zr/Ti)-X (X: NH_2 or NO_2) in their series. In short, in terms of photocatalyst decay relaxation dynamics both fs- and ns-TAS serve as indicators of charge separation efficiency and agree with the order observed in their photocatalytic activity.

To further evaluate the photoinduced charge separation efficiency of UiO-66 solids and their relationship with their photocatalytic activities, photocatalysts were characterized by PL spectroscopy, transient photocurrent and EIS measurements. PL spectroscopy is commonly used in heterogeneous photocatalysis, including MOFs, to evaluate the photoexcited charge transfer and recombination processes [85, 86]. Amino functionalized UiO-66 solids have a different degree of fluorescence while negligible emission was found when using the nitro functionalized solids. These results agree with some of our previous results showing that acetonitrile solutions of 2-aminoterephthalate emit much more on excitation at 266 nm than the analogous 2-nitroterephthalate acetonitrile solutions [55]. Figure 8a shows that the UiO-66(Zr/Ti)-NH_2 suspension has lower emissions than UiO-66(Zr)-NH_2, which agrees with similar studies that highlighted the higher efficiency of photoinduced charge separation of mixed-metal UiO-66(Zr/Ti)-NH_2 solids, in which Ti(IV) atoms act as the electron mediator during the process [48]. Similar measurements using fresh or used RuO_x NPs supported UiO-66(Zr)-NH_2, and specially UiO-66(Zr/Ti)-NH_2 solids, produced considerably less fluorescence emission intensity. Regardless the much lower fluorescence emission intensity observed when using nitro-functionalized UiO-66-based solids compared to amino ones, analogous conclusions about the fluorescence quenching in mixed-metal solids with or without fresh

and used RuOx respect to the parent sample can be drawn (Figure 8b). These results indicate that the presence of RuO_x NPs in the UiO-66 solids reduces the recombination rate of photogenerated electron-hole pairs and thus increases the efficiency of photoinduced charge separation.

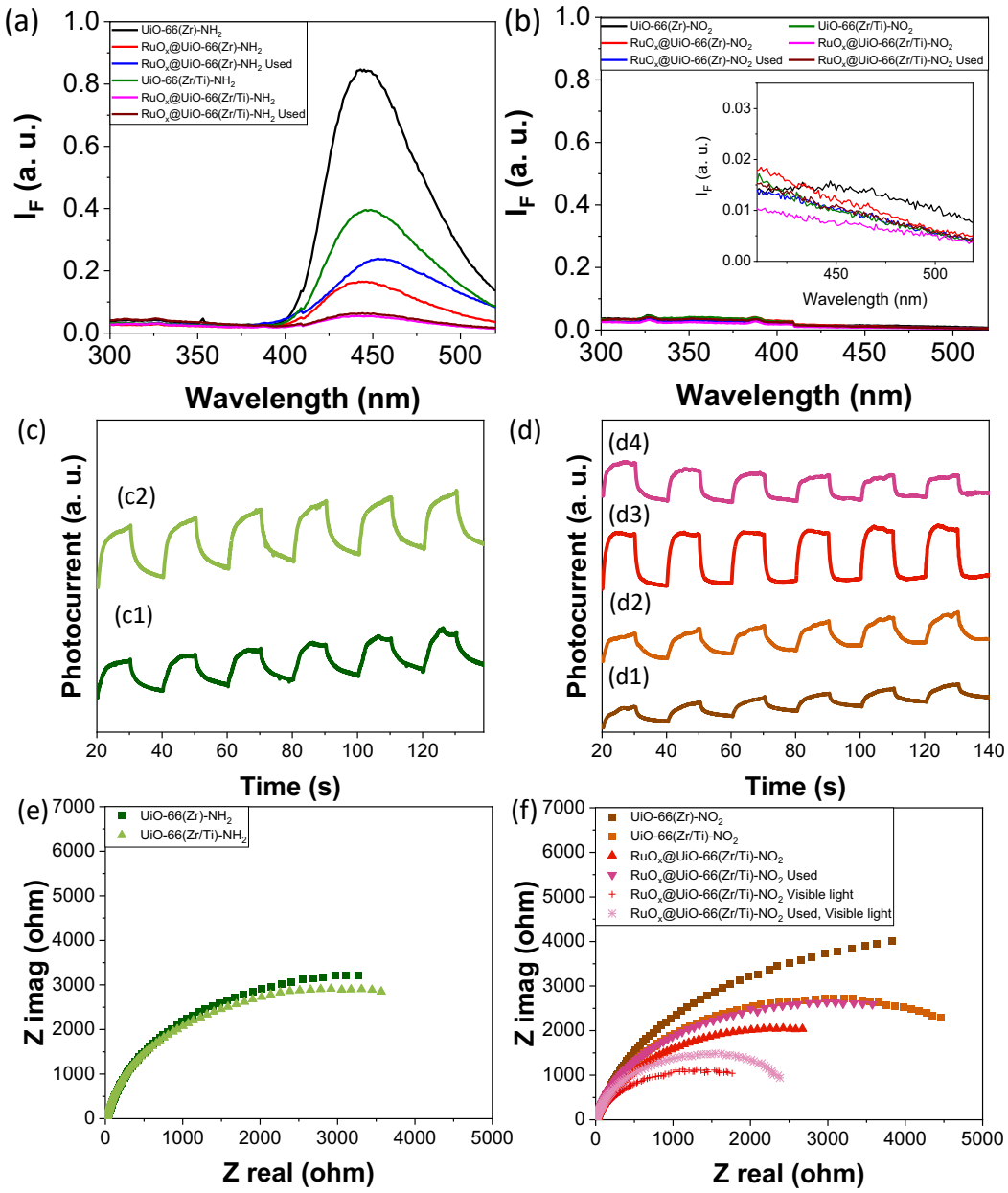

Figure 8. (a) PL measurements performed in acetonitrile MOF suspension having the same optical absorption (ca 35 a.u.) at 266 nm corresponding with the monochromatic excitation wavelength of the MOF organic. (b) Current intensity response of amino- (c)

or nitro-based (d) UiO-66 solids. Nyquist plots of amino- (e) or nitro-based (f) UiO-66 solids under dark or simulated concentrated sunlight irradiation as indicated. Legend: (c1) UiO-66(Zr)-NH_2, (c2) UiO-66(Zr/Ti)-NH_2, (d1) UiO-66(Zr)-NO_2, (d2) UiO-66(Zr/Ti)-NO_2, (d3) RuO_x@UiO-66(Zr/Ti)-NO_2 fresh, (d4) RuO_x@UiO-66(Zr/Ti)-NO_2 used.

The transient photocurrent results using UiO-66 solids under several on/off illumination cycles are shown in Figure 8. For these measurements, UiO-based photocatalysts were supported on a carbon substrate electrode and used in a standard three-electrode electrochemical cell as a working electrode previously polarized at + 0.9 V. The results show that mixed-metal UiO-66 solids have higher photocurrent intensities than monometallic ones (Figure 8). Analogous measurements using used and fresh RuO_x@UiO-66(Zr/Ti)-NO_2 photocatalysts found higher current intensities in simulated concentrated sunlight illumination and indicated an improvement in charge separation efficiency. An additional experiment using fresh RuO_x@UiO-66(Zr/Ti)-NO_2 in the presence of methanol gave a 5-fold enhancement of current intensity (Figure S49). This was due to the oxidation of methanol in the photogenerated holes that partially avoided electron recombination, so that a higher current intensity was measured than in the experiment with pure acetonitrile as solvent.

PL and transient photocurrent conclusions were complemented by EIS measurements (Figure 8). The smallest Nyquist arc radii were obtained from the most active samples of the series with the lowest charge transfer resistance. PL, transient photocurrent and EIS measurements showed that titanium ions in the metal nodes of UiO-66(Zr/Ti) and/or RuO_x@UiO-66 solids acted as electron mediators during the photoinduced electron transfer from the organic ligand to the metal node and increased the process efficiency [48, 86].

Previous studies reported the use of solid-state ESR spectroscopy to characterize the formation of photoactive reductive sites in MOFs like UiO-66(Zr)-NH_2 [55, 59] or MIL-125(Ti)-NH_2. For example, it has been reported that irradiation of UiO-66(Zr)-NH_2 results in photoinduced charge separation from the organic ligand to the metal node and the transformation of Zr(IV) species into Zr(III) species while the holes are located in the organic ligand [55, 59, 87]. Other studies have proposed that the irradiation of mixed-metal UiO-66(Zr/Ti)-NH_2 produces an LMCT mechanism with the initial reduction of Ti(IV) to Ti(III) in Ti(III)-O-Zr(IV) metal nodes, which are later transformed into Ti(IV)-O-Zr(III) [48]. These studies highlight the role of Ti(IV) species in mixed-metal UiO-66 solids as electron mediators from excited organic ligands that favor charge separation. In the present study, solid-state ESR experiments were carried out using UiO-66(Zr)-X (X: NH_2 or NO_2) and the analogous mixed-metals UiO-66(Zr/Ti)-X (X: NH_2 or NO_2) (Figures 9 and S50). Control solid-state ESR experiments in dark conditions revealed the presence of some paramagnetic signals in amino-functionalized UiO-66, associated with the presence of Zr(III) species that, however, are absent in analogous nitro solids, in agreement with previous related studies [55]. Irradiation of mono- or bimetallic UiO-66 solids functionalized with either amino or nitro groups in all cases produce the formation of an ESR band with g value of 2.004, characteristic of the Zr(III) species. These experiments indicate the occurrence of LMCT mechanisms in MOFs, while the absence of ESR Ti(III) signals could be associated with the previously proposed fast kinetics of metal electron transfer from Ti(III) as electron mediator to geminal Zr(IV) [48].

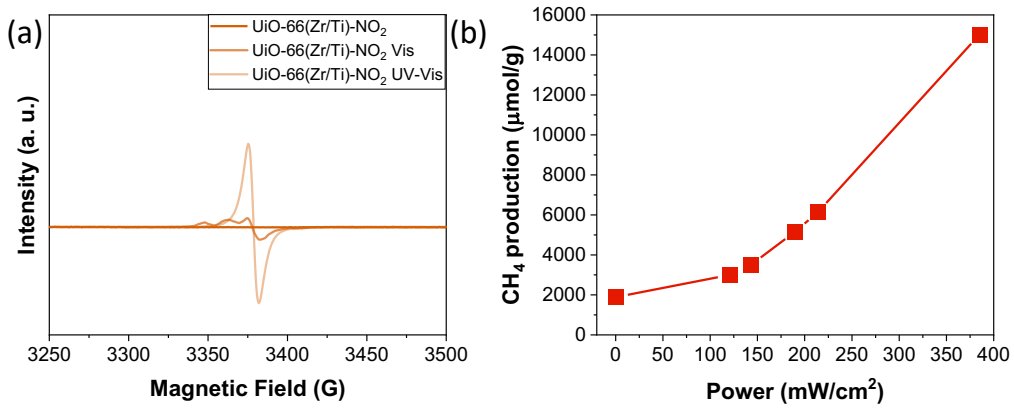

Figure 9. (a) EPR of solid UiO-66(Zr/Ti)-NO_2 after different irradiation conditions as indicated; (b) Influence of simulated light intensity into photocatalytic CH_4 formation.

Based on previous studies and due to the use of RuO_x NPs as co-catalysts during photocatalytic CO_2 reduction, the occurrence of a photothermal pathway can be hypothesized in which light energy is transformed into heat energy [77-79]. An indirect experiment to determine this possible pathway was conducted by evaluating photocatalytic CO_2 methanation as a function of the simulated sunlight intensity. Figure 9 shows that photocatalytic methane production increases linearly as a function of irradiance intensity up to about 125 mW/cm^2 and then an exponential relationship can be seen. These results are interpreted as the occurrence of a photothermal reaction pathway, especially at high irradiance intensities, in which light irradiation is transformed into local heat in RuO_x NPs, promoting CO_2 hydrogenation to CH_4.

The measurement of catalyst temperature during the photothermal reaction is of great importance to understand the thermal- and non-thermal contributions of the whole process [88]. To address this challenge measurement several techniques have been reported like direct measurement with a thermocouple, or non-contact techniques with infrared sensors or thermal cameras[88]. Other common method to assess catalyst local heating is based on the use of supported inorganic quantum dots (QDs) as temperature sensor with

optical readout [26, 89]. Specifically, the measurement of PL emission decrease of supported inorganic quantum dots (QDs) on a photocatalyst is a function of the local temperature [26, 43]. In this work, commercially available CdSe-ZnS QDs were employed as local nanothermometers. The series of PL experiments upon CdSe-ZnS QDs excitation at 450 nm were performed at temperatures from 200 to 280 ºC under dark or upon simulated sunlight irradiation intensities from 85 to 385 mW/cm^2. Figure S51 shows that the characteristic PL emission band of CdSe-ZnS QDs centered about 540 nm gradually decreases as the temperature increases. These experiments confirmed the possibility of using these CdSe-ZnS QDs as local nanothermometers in agreement with previous reports [26, 43]. Additionally, the PL emission intensity of CdSe-ZnS QDs recorded at 200 ºC also decreased upon irradiation, the highest the irradiation intensity the highest the PL quenching and associated to the local heating of CdSe-ZnS QDs upon irradiation. Analogous PL results were obtained in the case of used RuO_x@UiO-66(Zr/Ti)-NO_2 photocatalyst supported CdSe/ZnS QDs deposited on a quartz holder as a function of either the temperature or the simulated sunlight irradiation at different irradiances. It should be noted that during these PL experiments negligible temperature changes of the sample upon different irradiations were measured using an infrared thermometer. Therefore, it is likely to propose that the observed PL quenching upon irradiation might be associated with a photocatalyst local heating due to irradiation. Overall, these PL results together with those ones shown in Figure 9 about the influence of simulated light intensity into photocatalytic CH_4 formation would agree with the occurrence of a photothermal reaction pathway during CO_2 reduction.

Further investigation of the photothermal behavior was conducted by monitoring the IR bands shift of the structural bands using Operando FTIR experiment under different temperatures, given the fact as temperature increases the molecular vibration of the

different species increases resulting IR bands shift . Results confirms this behavior on the RuOx@UiO-66(Zr/Ti)-NO_2 showing a structural band shift from 3668 to 3664 cm^{-1} (assigned to OH vibration) as temperature increased from 100 to 200 °C under dark conditions (inset of figure 8b A). This effect was then investigated for the reaction under irradiation at room temperature (RT). Interestingly, a significant band shift from 3369 to 3360 cm^{-1}**(Figure 8b B**) is observed indicating a potential localized temperature increase (estimated of around 145 °C). However, at elevated temperature (200 °C) this effect was diminished whereby a lower band shift is observed (Figure 8b C). This result is consitent with that of the PL quenching of the quantum dote. Moreover, it's important to highlight that no activity was observed at room temperature under irradiation in our reaction conditions, unlike the result obtained at 125°C in darkness under similar conditions(see. This indicates that this phenomenon is unlikely to be the primary determinant of the sample's activity.

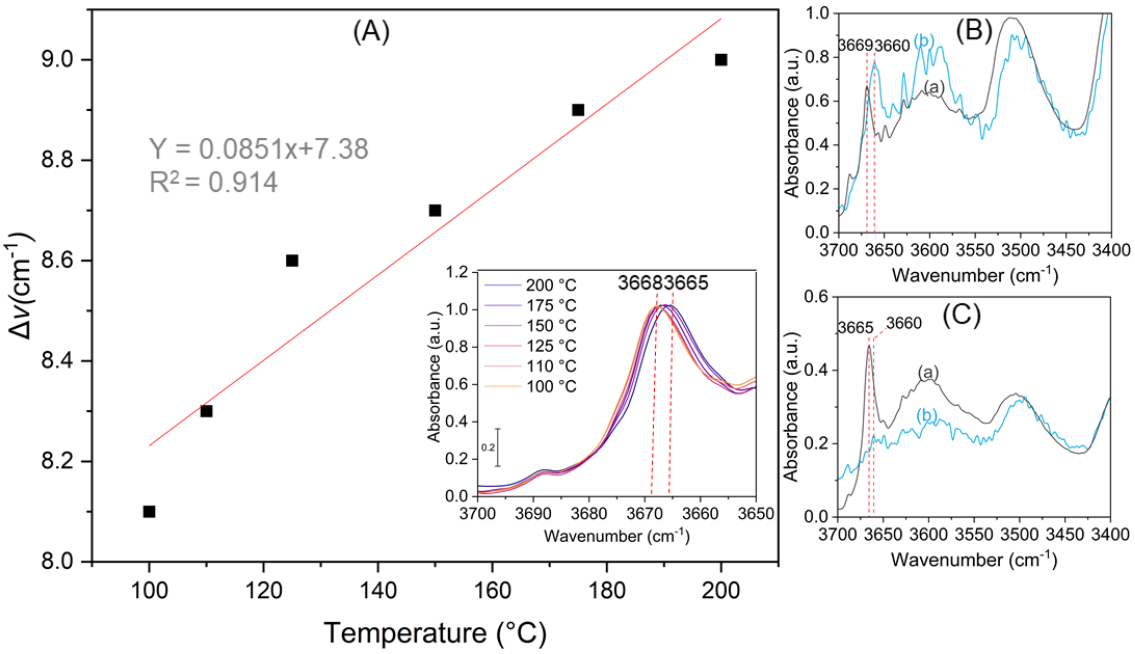

Figure 8b.(A) Evolution of the structral band shift as function of temperature (inset: Direct surfce FTIR spectra of RuO_x@UiO-66(Zr/Ti)-NO_2 in the 3700-3650 region at

different temperatures in dark), (B) and (C) FTIR spectra in the same region (a)in dark and (b)under irradtion at 30 °C and 200 °C respectively. Spectra collected under contineous flow of Ar (20 cm^3/min).

Overall, RuO_x NPs supported UiO-66(Zr/Ti)-NO_2 generally acts as a multifunctional photocatalyst during CO_2 methanation under simulated concentrated sunlight irradiation (Figure 10). During the photochemical pathway irradiation of the photocatalyst, we consider that a photoinduced electron transfer from the organic ligand to the metal-oxo cluster takes place. These electrons can be further transferred to RuO_x NPs, where CO_2 methanation occurs. Irradiation can also promote the heating of RuO_x NPs CO_2 hydrogenation to methane.

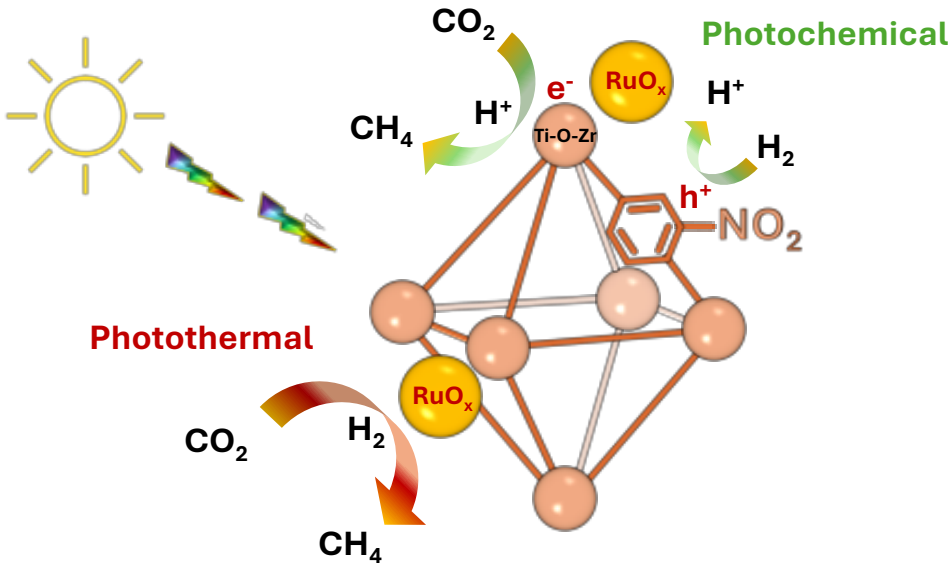

Figure 10. Proposed reaction mechanism during CO_2 methanation using RuO_x@UiO-66(Zr/Ti)-NO_2 as multifunctional photocatalyst. (to be changed by Celia)

3.3.2. Evaluation of photocatalytic CO_2 hydrogenation to CH_4

The previous photocatalytic results using UiO-66-based materials have shown a selective CO_2 hydrogenation to CH_4. These results agree with analogous studies reporting that the use of supported RuO_x NPs facilitates chemisorption of CO_2 and their reaction intermediates and promote the (photo)catalytic hydrogenation to methane [90-92]. To shed some light on the CO_2 and CO adsorption capacity aver RuO_x@UiO-66(Zr/Ti)-NO_2 topic, CO_2 and CO adsorption experiments were conducted under continuous flow of CO_2/Ar and CO/Ar under *operando* conditions and the results were analyzed through IR. Initially, different concentrations of CO_2 were introduced in Ar with a total flow rate of 20 $cm^3.min^{-1}$. It is witnessed that as the concentration of CO_2 increases, the band centered at 2238 cm^{-1} characteristic of chemisorbed CO_2 increases in a linear way, as illustrated in **figure 11 A**. The results are presented after subtraction of gaseous CO_2 phase. Direct spectra can be found in the SI (figure S54 A). Upon reaching saturation, CO_2 adsorption was investigated as a function of the temperature (as depicted in **figure 11 B**). These results demonstrated an exponential decrease in chemisorbed CO_2 concentration as the temperature increases, until reaching 30 °C. Subsequently, the enthalpy and entropy of this reaction were calculated based on the linear relationship of $\mathrm{Ln}\left[\frac{nCO_2\ (T=T_n)}{nCO_2(T=298)-nCO_2(T=T_n)} \times \frac{P}{P_0}\right]$ (where nCO2 represents the number of moles of chemisorbed CO_2, T_n is the temperature reached at each point, and P/P_0 is the relative pressure of CO_2 in Ar) as a function of the inverse of temperature (-1/T), as shown in **figure 11 C**. The enthalpy of the reaction was determined from the slope of the line and equal to -22.5 kJ/mol, indicating relativelly weak and reversible adsorption of CO_2 on the catalyst surface. The investigation of CO adsorption on supported ruthenium catalysts holds significance not only for understanding the mechanism of CO_2 methanation reaction (considering that CO is one of the potential intermediates of this reaction) but

also for the characterization of their surface properties. CO serves as a prominent probe molecule, unveiling both the oxidation state and coordination environment of the sites to which it binds. **Figure 11 D** shows the evolution of the FTIR spectra of the RuO_x@UiO-66(Zr/Ti)-NO_2, in the CO vibration spectral region (2200-1800 cm^{-1}), upon the introduction of 0.05% CO in Ar to the sample preactivated under hydrogen at 200 °C. The results are subtracted from the spectrum after activation at room temperature -direct spectra can be found in the figure S54B. Different bands appeared on the surface, however, their assignment to specific adsorption sites is not straightforward, as witnessed by the different interpretations found in the literature. This variability likely arises from multiple factors influencing exact band positions, such as the coverage of CO and O, as well as the oxidation state of the adsorption site. According to literature findings, carbonyl species can predominantly be categorized into two distinct surface complexes: the spectral peaks at 2124 cm^{-1}, coupled with a component at 2055 cm^{-1}, are attributed to the asymmetric and symmetric stretching vibrations of an $Ru^{3+}(CO)_2$ species on the proximity of ZrO_2. Meanwhile, the spectral peaks at 2070 cm^{-1} and 2004 cm^{-1} are associated to those of $Ru^{2+}(CO)_2$ species. Furthermore, peaks at lower wavenumbers (1995, 1987 and 1955 cm^{-1}) may be attributed to monocarbonyls adsorbed on less oxidized $Ru^{\delta+}$ supported on TiO_2. Furthermore, a less intense peak at 2023 cm^{-1} may be attributed to CO linearly bound to metallic Ru^0. The approximative assignments of the spectral bands are summarized in table S3

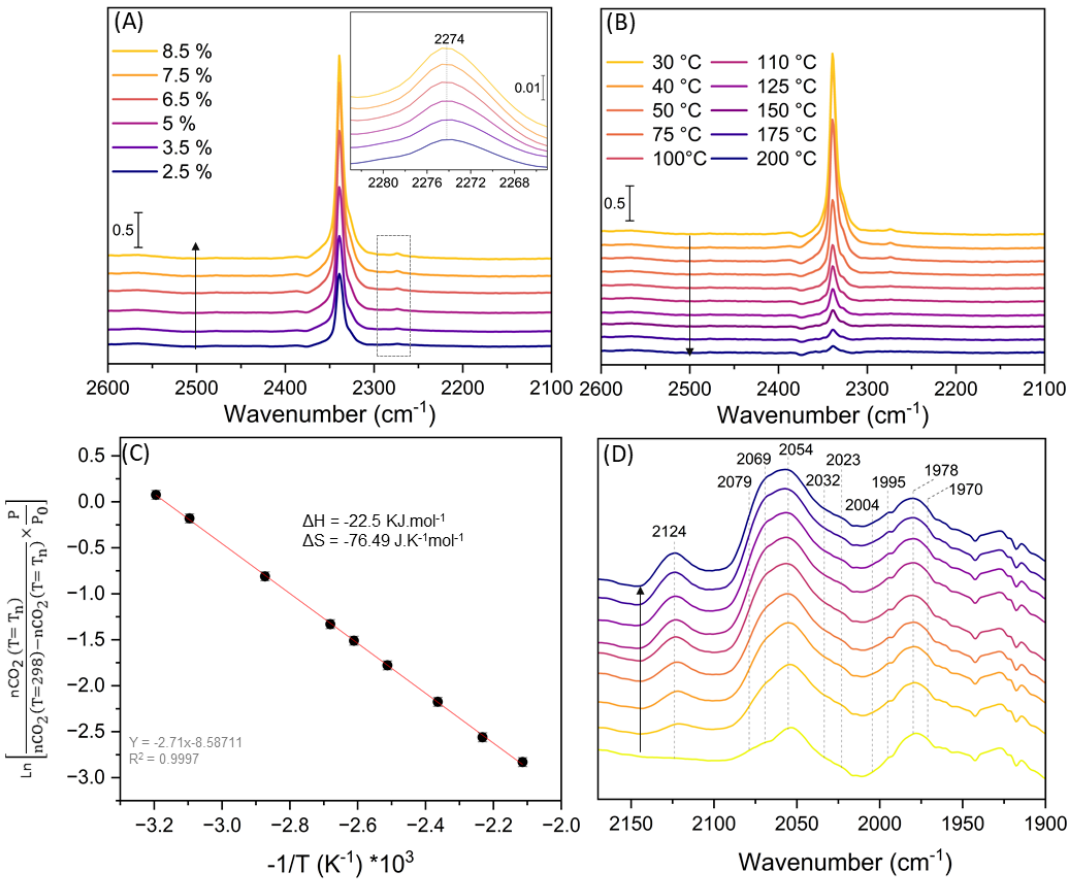

Figure 11. (A, B) FTIR spectra of chemisorbed CO_2 on RuO_x@UiO-66(Zr/Ti)-NO_2 versus different concentration of CO_2 in Argon and temperature respectively (total flow rate = 20 $cm^3.min^{-1}$), (C)the corresponding enthalpy and the entropy of the CO_2 chemisorption, and (D) Evolution of FTIR spectra of adsorbed CO on RuO_x@UiO-66(Zr/Ti)-NO_2 in the 2150-1900 cm^{-1}

The performance of the most active RuO_x@UiO-66(Zr/Ti)-NO_2 sample during photocatalytic CO_2 hydrogenation to CH_4 was further investigated through *operando* FTIR experiments where both the gas phase products and the surface of the catalyst are analyzed simultaneously in real time under similar irradiation conditions used previously in batch. More details on the operando approach can be found in the references. The setup is equipped with online mass spectrometer (MS) and gas chromatography (GC) whereby online injections are taken throughout the reaction. A "Sandwich" cell reactor (**Figure 12**

A) was used to carry out these experiments where the catalyst is fixed in the cell as a self-supported pallet (20 mg). The sample was first activated under hydrogen at 200 °C then its activity for the CO_2 methanation was assessed with a molar ratio of 4:1 of H_2 to CO_2 with a total flow rate of 10 $cm^3.min^{-1}$ The photo-thermal CO_2 methanation activity of RuO_x@UiO-66(Zr/Ti)-NO_2 was tested under different temperatures (**Figure 12 B, C**). No methane production was detected at 30 °C, either in darkness or under visible light irradiation, as evidenced by the analysis of the gas phase at the steady-state. However, upon reaching 75 °C, methane production increased with rising temperature in the absence of light. Interestingly, under irradiation, methane production exhibited a significant increase with increasing temperature, reaching 8 $mmol \cdot g^{-1} \cdot h^{-1}$ at 200 °C, with a selectivity of 98.1%. This observation was further confirmed by FTIR analysis, which revealed only CH_4 and H_2O as gas phase products (**Figure 12B).** Complementary results of the GC analysis showed, in addition to methane, the production of ethylene and propylene (under the detection limit of our FTIR-gas analysis) as side products with a selectivity of 1.65 % and 0.27 % respectively **(inset of Figure 12 C).** Subsequently, an investigation into the impact of lamp intensity on the activity of RuOx@UiO-66(Zr/Ti)-NO_2 was carried out at 200 °C, as illustrated in **Figure 12 D**. The sample's activity decreased in quasi-linear manner from 8.7 to 3.5 $mmol.g^{-1}.h^{-1}$ as the relative intensity of the lamp decreased from 100 to 20 % I_0. No significant deactivation was observed in agreement with the previous experiments that were conducted in batch conditions at different simulated sunlight irradiation intensities. The decline in the sample's activity with decreasing lamp intensity suggests a diminished prominence of plasmonic effects during the reaction under irradiation. This indicates that the catalytic behavior may be governed by factors beyond predominant plasmonic-mediated mechanisms.

In an attempt to gain more information of the underlying mechanism of the CO_2 hydrogenation over the RuOx@UiO-66(Zr/Ti)-NO_2, the surface of the catalyst was simultaneously monitored by FTIR during the reaction. The IR spectra of the surface, at steady state, between 30 and 200 °C are shown in **Figure 12 E**. Results are subtracted from the spectrum at 30 °C of the preactivated sample. It's essential to note that the spectral regions corresponding to stretching vibration of formates and carbonates, specifically between 1600 and 1300 cm^{-1}, are saturated. Therefore, for assigning the different possible reaction intermediates, both the CO vibrational region and the unobstructed region between 1200 and 1000 cm^{-1} are taken into consideration. Different bands emerged as temperature increased in the CO region mainly at 2088 and 1985 cm^{-1} possibly attributed to adsorbed CO on $Ru^{\delta+}$ on the proximity of TiO_2. Furthermore, a band emerged as temperature increased from 30 to 75 °C at 2016 cm^{-1} after which it diminished. This decrease was accompanied with the start of the methane production at 75 °C (**Figure 12B** curve d). This band could be attributed to CO linearly adsorbed on Ru^0. These results indicates that the formation of CO on the surface is promoted at lower temperatures even if no methane is produced yet. The no detection of CO in gas phase at high temperature, emphasizes its key role as an intermediate in the CO_2 methanation reaction over RuO_x@UiO-66(Zr/Ti)-NO_2. At higher temperatures, the formation of formyl as an intermediate was suggested by the presence of the band at 1175 cm^{-1} . Furthermore, various bands corresponding to methoxy species are observed in the spectra at 1160 (on-top) and 1060 (doubly bridging) cm^{-1} owing to the stretching vibrations of methoxys. Also, a band at 1130 cm^{-1} elevated as temperature increased that probably attributed to dioxymethylene adsorbed on the surface. It is important to mention that increasing the temperature causes a shift in the vibrational bands of species present on the surface, justifying the negative signals on the subtracted spectra.

To confirm involvement of the various species in the reaction mechanism and their intermediates role a steady state isotopic transient kinetic analysis (SSITKA) experiment using operando FTIR spectroscopy was performed at 200°C. It corresponds to replacing $^{12}CO_2$ by its isotope $^{13}CO_2$ at steady state under the same reaction conditions. The isotopic transient leads to shift of the IR bands of the surface intermediates as well as their corresponding final. Additionally, this approach ensures that any observed shift would solely result from isotopic exchange between $^{13}CO_2$ and $^{12}CO_2$ and not due to the change of temperature and structural band's shift. However due to the fact that pure $^{13}CO_2$ is very expensive, this experiment was carried out under diluted conditions (1% of $^{12}CO_2$ in Argon then exchange to 1% of $^{13}CO_2$ in Argon). Interestingly $^{13}CH_4$ was produced selectively with $^{13}CO_2$ with a similar quantity to that produced with $^{12}CO_2$ (**Figure 12 G**). This was accompanied with the shift (3 or 4 cm^{-1}; table S4) in IR bands of different species previously attributed to CO, formyl, methoxy, and dioxymethylene with $^{13}CO_2$, as depicted in **Figure 12 F.** Therefore, these confirms the role of these species as reaction intermediates. It should be noted that due to the overlap with the CO vibration, it was difficult to distinguish the band related to the hydride bond formed by hydrogen dissociation on reduced Ru.

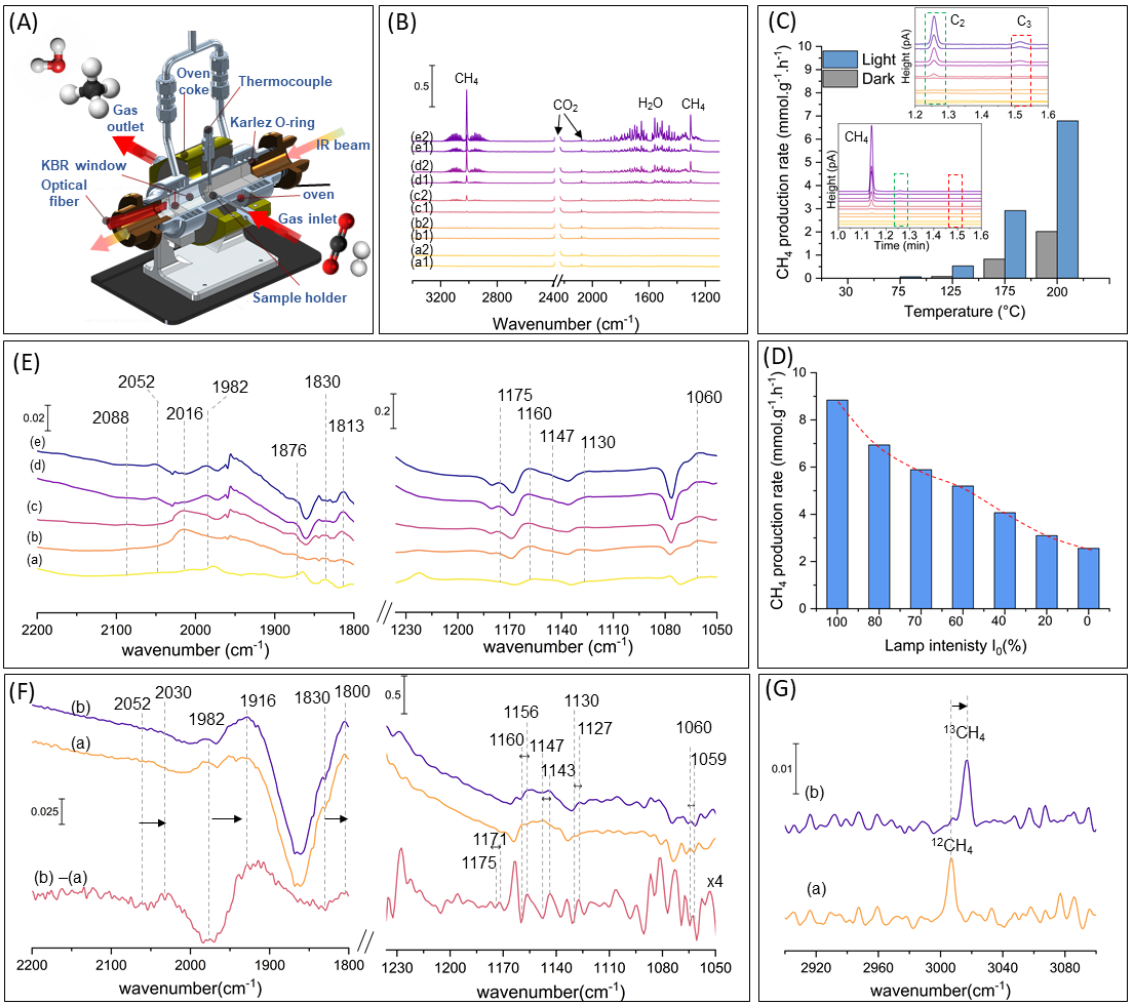

Figure.12 (A) Sandwich IR Reactor-cell used for studying the CO_2 methanation reaction under visible light in continuous flow. (B) the FTIR spectra of the reaction gas phase : (a) 30, (b) 75, (c) 125, (d) 175 and (e) 200 °C with (1) in dark and (2) after irradiation at steady state, (C) activity of RuO_x@UiO-66(Zr/Ti)-NO_2 as function of temperature in dark and under visible light irradiation (inset: gas chromatography chromatograms of the reaction gas phase under same conditions). (D) *Operando* FTIR spectra of RuO_x@UiO-66(Zr/Ti)-NO_2 versus temperature: (a) 30, (b) 75, (c) 125, (d) 175 and (e) 200 °C in the 2200-1800 and the 1200-1000 cm^{-1} vibrational regions. (E) activity of RuO_x@UiO-66(Zr/Ti)-NO_2 as function of lamp intensity. (F) FTIR spectra of the catalyst during the photoassisted methanation at 200°C of (a) $^{13}CO_2$ and (b) $^{12}CO_2$ and the corresponding subtracted spectrum ($^{13}CO_2$ - $^{12}CO_2$) is presented in (c) (intensity was multiplied by four

for clarity. (G) FTIR gas phase spectra of gaseous methane produced during the photoassisted methanation of (a)$^{12}CO_2$ and (b)$^{13}CO_2$ at 200°C. The arrow corresponds ro shift of the IR bands due to the isotopic exchange from $^{12}CO_2$ to $^{13}CO_2$. The assigments of the different IR bands are summarized in table. S3 and S4.

Based on the spectral investigations mentioned above, a proposed overall mechanism for the reaction unfolds as illustrated in scheme X : Initially, CO_2 is adsorbed on the surface, primarily on Ru species, accompanied with a hydride formation of reduced Ru. Subsequently, CO is generated as the primary intermediate of CO_2 reduction, which exhibits strong surface adsorption. This is evident from the absence of CO as final product in the gas phase, as confirmed by FTIR and GC analyses (**see Figure 12 B, C**). As temperature increases, the photoassisted reduction of CO to formyl is promoted, followed by its conversion to dioxymethylene through interaction with surface oxygen. Then, the photoassisted reduction of dioxymethylene produces methoxy as the final intermediate species before generating methane and water as final products through further reduction. This mechansim emphasizes the dual role of RuO_x and reduced Ru in the production of methane from CO_2 and H_2.

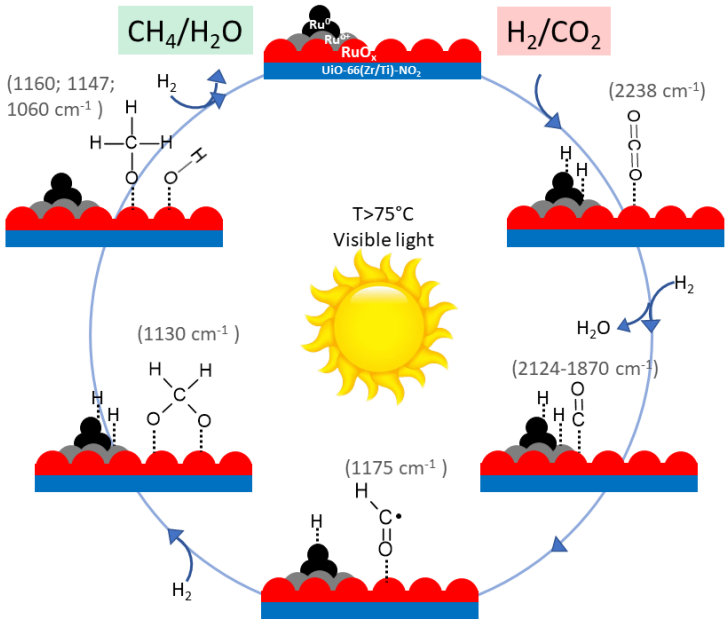

Scheme X. The proposed mechanism of the photo-assisted CO_2 methanation over RuO_x@UiO-66(Zr/Ti)-NO_2 based on the assignment of the characteristic IR bands of the various species.

4. Conclusions

This study describes the development of multifunctional and photocatalytically active UiO-66 solids supported RuO_x NPs (2 ±0.1 nm) for CO_2 methanation at 200 ºC under simulated concentrated sunlight irradiation. The photocatalytic activity of the samples followed the order UiO-66(Zr/Ti)-NO_2 > UiO-66(Zr/Ti)-NH_2 ~ UiO-66(Zr)-NO_2 > UiO-66(Zr)-NH_2. In contrast to most reports involving UiO-66 photocatalysts based on the use of the 2-aminoterephthalate ligand, the present study highlights the importance of using 2-nitroterephthalate ligands to achieve high activity with Zr(IV) or mixed-metal Zr(IV)/Ti(IV) nodes within UiO-66 based materials and associated with the unique energy band level diagram of these solids. It should be noted that UiO-66(Zr/Ti)-NO_2 is a reusable photocatalyst that exhibits record activity (5.03 mmol g^{-1} after 22 h; AQY at 350, 400 and 600 nm of 1.67, 0.25 and 0.01, respectively) compared to previous analogous reports on MOF-based materials. Based on the results of several spectroscopic, electrochemical and photocatalytic experiments, we consider that RuO_x@ UiO-66(Zr/Ti)-NO_2 operates in a dual photochemical and photothermal reaction pathway. The photocatalytic CO_2 hydrogenation pathway was further investigated in flow condition using operando FT-IR spectroscopy. The results are in very good agreement with that obtained in batch conditions. Basing on the surface analysis and SSITKA experiment, a mechanism involving CO, formyl, dioxomethane, and methoxy, as intermediates, has been illustrated. In summary, we propose an innovative combination of nitro functionalized UiO-66 solids with mixed-metal Zr(IV)/Ti(IV) nodes and supported RuO_x

NPs as co-catalyst to progress towards solar-driven photocatalytic CO_2 methanation. The authors consider that this work will open new possibilities for the development of multifunctional MOFs as solar-driven photocatalysts for selective CO_2 transformations.

The Supporting Information is available free of charge. Synthesis of the MOF-based materials, characterization techniques, photocatalytic activity. SEM and SEM-EDX mapping images, TEM images, XPS spectra, isothermal N_2 adsorption graphs, TGA analyses, UV-Vis diffuse reflectance spectra, Valence band XPS spectra, PXRD, mass spectrum of $^{17}CH_4$, femtosecond transient absorption spectra and decay traces, LFP spectra and decay traces, transient photocurrent plot, EPR spectra, Caen possible figures here, Table S1 (Photocatalytic CO_2 methanation by H_2 using MOF-based photocatalysts reported in the literature), Table S2 (Global fit analysis)

Acknowledgements

C.M.R.N. thanks the support of PRE2019-089877 funded by MCIN/AEI /10.13039/501100011033. I.V. thanks the support of grant PID2020-115010RB-I00 funded by MCIN/AEI/10.13039/501100011033. A.L. thanks the support from the MICIN through grant PID2021-127918NB-I00. V.M.M. thanks financial support of grants PID2020-114347RB-C32, funded by MCIN/AEI/10.13039/501100011033 as well as Vasco-Eusko Jaurlaritza (project IT1639-22) and by ERDF A way of making Europe. S. N. thanks the support of grant PID2021-123856OBI00 funded by MICIU/AEI/10.13039/501100011033 and by ERDF A way of making Europe.

References

(1) Bosa, K.; Gupta, J. Stranded assets and stranded resources: Implications for climate change mitigation and global sustainable development. *Energy Res. Soc. Sci.* **2019**, *56*, 101215. https://doi.org/101210.101016/j.erss.102019.101205.101025.
(2) Paraschiv, S.; Paraschiv, L. S. Trends of carbon dioxide (CO2) emissions from fossil fuels combustion (coal, gas and oil) in the EU member states from 1960 to 2018. *Energy Rep.* **2020** *6*,237-242. https://doi.org/210.1016/j.egyr.2020.1011.1116.
(3) Østergaard, P. A.; Duic, N.; Noorollahi, Y.; Mikulcic, H.; Kalogirou, S. Sustainable development using renewable energy technology. *Renew. Energ.* **2020**, *146*, 2430–2437.
(4) Sherwood, J. The significance of biomass in a circular economy. *Bioresour. Technol.* **2020**, *300*, 122755.
(5) Radovanović, M.; Filipović, S.; Vukadinović, S.; Trbojević, M.; Podbregar, I. Decarbonisation of eastern European economies: monitoring, economic, social and security concerns. *Energy Sustain. Soc.* **2022**, *12*, 16. https://doi.org/10.1186/s13705-13022-00342-13708.
(6) de Kleijne, K.; Hanssen, S. V.; van Dinteren, L.; Huijbregts, M. A. J.; van Zelm, R.; de Coninck, H. Limits to Paris compatibility of CO2 capture and utilization. *One Earth* **2022**, *5*, 168-185. https://doi.org/110.1016/j.oneear.2022.1001.1006.
(7) Mac Dowell, N. F., P.S.; Shah, N.; Maitland, G.C. The role of CO2 capture and utilization in mitigating climate change. *Nat. Clim. Change* **2017**, *7* (243-249).
(8) Mikkelsen, M.; Jørgensen, M.; Krebs, F. C. The teraton challenge. A review of fixation and transformation of carbon dioxide. *Energ. Environ. Sci.* **2010**, *3*, 43-81. https://doi.org/10.1039/B912904A.
(9) Ding, M.; Flaig, R. W.; Jiang, H.-L.; Yaghi, O. M. Carbon capture and conversion using metal–organic frameworks and MOF-based materials. *Chem. Soc. Rev.* **2019**, *48*, 2783-2828.
(10) Zhang, Z.; Pan, S.-Y.; Li, H.; Cai, J.; Olabi, A. G.; Anthony, E. J.; Manovic, V. Recent advances in carbon dioxide utilization. *Renewable Sustainable Energy Rev.* **2020**, *125*, 109799. https://doi.org/109710.101016/j.rser.102020.109799.
(11) Artz, J.; Müller, T. E.; Thenert, K.; Kleinekorte, J.; Meys, R.; Sternberg, A.; Bardow, A.; Leitner, W. Sustainable conversion of carbon dioxide: An integrated review of catalysis and life cycle assessment. *Chem. Rev.* **2018**, *118*, 434–504. https://doi.org/410.1021/acs.chemrev.1027b00435.
(12) Dhakshinamoorthy, A. N., S.; Primo, A.; García, H. Selective gas-phase hydrogenation of CO2 to methanol catalysed by metal-organic frameworks. *Angew. Chem. Int. Ed.* **2023**, https://doi.org/10.1002/anie.202311241.
(13) Bellabarba, R.; Johnston, P.; Moss, S.; Sievers; C.; B., S.; Tway, C.; Wang, Z.; Zhu, H. Net zero transition: possible implications for catalysis. *ACS Catal.* **2023**, *13*, 7917–7928.
(14) De, S. D., A.; Ramirez, A.; Gascon, J. Advances in the design of heterogeneous catalysts and thermocatalytic processes for CO2 utilization. *ACS Catal.* **2020**, *10*, 14147-14185.
(15) Lin, H.; Luo, S.; Zhang, H.; Ye, J. Toward solar-driven carbon recycling. *Joule* **2022**, *6*, 294–314. https://doi.org/210.1016/j.joule.2022.1001.1001.
(16) Lewis, N. S. Research opportunities to advance solar energy utilization. *Science* **2016**, *351*, 1920.
(17) Lewis, N. S.; Nocera, D. G. Powering the planet: Chemical challenges in solar energy utilization. *Proc. Natl. Acad. Sci. USA* **2006**, *103*, 15729-15735.
(18) Ciocarlan, R.-G. B., N.; Lenaerts, S.; Cool, P.; Verbruggen, S.W. Recent trends in plasmon-assisted photocatalytic CO2 reduction. *ChemSusChem* **2023**, *16*, 202201647.
(19) Wang, Q.; Domen, K. Particulate photocatalysts for light-driven water splitting: Mechanisms, challenges, and design strategies. *Chem. Rev.* **2020**, *120*, 919-985.

(20) Halmann, M. Photoelectrochemical reduction of aqueous carbon dioxide on p-type gallium phosphide in liquid junction solar cells. *Nature* **1978**, *275*, 115–116.
(21) Thampi, K. R.; Kiwi, J.; Graetzel, M. Methanation and photo-methanation of carbondioxide at room-temperature and atmospheric-pressure, . *Nature* **1987**, *327*, 506-508. https://doi.org/510.1038/327506a327500.
(22) Chen, D.; Zhang, X.; Lee, A. F. Synthetic strategies to nanostructured photocatalysts for CO2 reduction to solar fuels and chemicals. *J. Mater. Chem. A* **2015**, *3*, 14487-14516. DOI https://doi.org/14410.11039/C14485TA01592H.
(23) Li, X.; Yu, J.; Jaroniec, M.; Chen, X. Cocatalysts for selective photoreduction of CO2 into solar fuels. *Chem. Rev.* **2019**, *119*, 3962−4179. https://doi.org/3910.1021/acs.chemrev.3968b00400.
(24) Ulmer, U.; Dingle, T.; Duchesne, P. N.; Morris, R. H.; Tavasoli, A.; Wood, T.; Ozin, G. A. Fundamentals and applications of photocatalytic CO2 methanation. *Nat. Commun.* **2019**, *10*, 3169.
(25) Mateo, D.; Albero, J.; Garcıa, H. Titanium-perovskite-supported RuO2 nanoparticles for photocatalytic CO2 methanation. *Joule* **2019**, *3*, 1949-1962. https://doi.org/1910.1016/j.joule.2019.1906.1001.
(26) Mateo, D.; Albero, J.; García, H. Photoassisted methanation using Cu2O nanoparticles supported on graphene as a photocatalyst. *Energy Environ. Sci.* **2017**, *10*, 2392-2400. https://doi.org/2310.1039/C2397EE02287E.
(27) Mateo, D.; Albero, J.; García, H. Graphene supported NiO/Ni nanoparticles as efficient photocatalyst for gas phase CO2 reduction with hydrogen. *Appl. Catal. B.-Environ.* **2018**, *224*, 563-571. https://doi.org/510.1016/j.apcatb.2017.1010.1071.
(28) Barrio, J.; Mateo, D.; Albero, J.; García, H.; Shalom, M. A heterogeneous carbon nitride–nickel photocatalyst for efficient low-temperature CO2 methanation. *Adv. Energy Mater.* **2019**, *9*, 1902738. https://doi.org/1902710.1901002/aenm.201902738.
(29) Jelle, A. A.; Ghuman, K. K.; O'Brien P.G.; Hmadeh, M.; Sandhel, A.; Perovic, C. D. D.; Singh, V.; Mims, C. A.; Ozin, G. A. Highly efficient ambient temperature CO2 photomethanation catalyzed by nanostructured RuO2 on silicon photonic crystal support. *Adv. Energy Mater.* **2018**, *8*, 1702277. https://doi.org/1702210.1701002/aenm.201702277.
(30) Albero, J.; Peng, Y.; García, H. Photocatalytic CO2 reduction to C2+ products. *ACS Catal.* **2020**, *10*, 5734-5749.
(31) Navalón, S. D., A.; Álvaro, M.; Ferrer, B.; García, H. Metal–organic frameworks as photocatalysts for solar-driven overall water splitting. *Chem. Rev.* **2023**, *123*, 445-490. https://doi.org/410.1021/acs.chemrev.1022c00460.
(32) Younas, M.; Loong Kong, L. L.; Bashir, M. J. K.; Nadeem, H.; Shehzad, A.; Sethupathi, S. Recent advancements, fundamental challenges, and opportunities in catalytic methanation of CO2. *Energ. Fuels* **2016**, *30*, 8815-8831. https://doi.org/8810.1021/acs.energyfuels.8816b01723.
(33) Walspurger, S.; Haije, W. G.; Louis, B. CO2 reduction to substitute natural gas: Toward a global low carbon energy system. *Isr. J. Chem.* **2014**, *54*, 1432-1442. https://doi.org/1410.1002/ijch.201300135.
(34) Khan, S. D., X.; Ali, T.; Mahmood, S.; ul Haq, M.; Sohail Riaz, M.; Hu, Y. Recent advances on photo-thermo-catalysis for carbon dioxide methanation, . *Int. J. Hydrog. Energy* **2022**, *48*, 24756-24787.
(35) Zhao, J. L., J.; Li, Z.; Wang, K.; Shi, R.; Wang, P.; Wang, Q.; Waterhouse, G.I.N; Wen, X.; Zhang, T. Ruthenium-cobalt single atom alloy for CO photo-hydrogenation to liquid fuels at ambient pressures. *Nat. Commun.* **2023**, *14*, 1909.
(36) Cabrero-Antonino, M.; Remiro-Buenamañana, S.; Souto, M.; García-Valdivia, A. A.; Choquesillo-Lazarte, D.; Navalón, S.; Rodríguez-Diéguez, A.; Mínguez-Espallargas, G.; García, H. Design of cost-efficient and photocatalytically active Zn-based MOFs

decorated with Cu2O nanoparticles for CO2 methanation. *Chem. Commun.* **2019**, *55*, 10932-10935. DOI https://doi.org/10910.11039/C10939CC04446A.
(37) Férey, G.; Mellot-Draznieks, C.; Serre, C.; Millange, F.; Dutour, J.; Surblé, S.; Margiolaki, I. A chromium terephthalate-based solid with unusually large pore volumes and surface area. *Science* **2005**, *23*, 2040-2042. 2010.1126/science.1116275.
(38) Furukawa, H.; Cordova, K. E.; O'Keeffe, M.; Yaghi, O. M. The chemistry and applications of metal-organic frameworks. *Science* **2013**, *341*, 1230444. 1230410.1231126/science.1231230.
(39) Kitagawa, S.; Kitaura, R.; Noro, S.-I. Functional porous coordination polymers. *Angew. Chem. Int. Ed.* **2004**, *43*, 2334-2375. https://doi.org/2310.1002/anie.200300610.
(40) Dhakshinamoorthy, A.; Asiri, A. M.; García, H. Metal-organic framework (MOF) compounds: Photocatalysts for redox reactions and solar fuel production. *Angew. Chem. Int. Ed.* **2016**, *55*, 5414-5445. https://doi.org/5410.1002/anie.201505581.
(41) Li, R.; Zhang, W.; Zhou, K. Metal–organic-framework-based catalysts for photoreduction of CO2. *Adv. Mater.* **2018**, *30*, 1705512. https://doi.org/1705510.1701002/adma.201705512.
(42) Kolobov, N.; Goesten, M. G.; Gascon, J. Metal–Organic Frameworks: Molecules or Semiconductors in Photocatalysis? . *Angew. Chem. Int. Ed.* **2021**, *60*, 26038-26052.
(43) Wang, S.; Cabrero-Antonino, M.; Navalón, S.; Chen-chen Cao, C.-c.; Tissot, A.; Dovgaliuk, I.; Marrot, J.; Martineau-Corcos, C.; Yu, L.; Wang, H.; et al. A robust titanium isophthalate metal-organic framework for visible-light photocatalytic CO2 methanation. *Chem* **2020**, *6*, 3409-3427. https://doi.org/3410.1016/j.chempr.2020.3410.3017.
(44) Cabrero-Antonino, M.; Ferrer, B.; Baldoví, H. G.; Navalón, S. Toward solar-driven photocatalytic CO2 methanation under continuous flow operation using benchmark MIL-125(Ti)-NH2 supported ruthenium nanoparticles. *Chem. Eng. J.* **2022**, *445*, 136426. https://doi.org/136410.131016/j.cej.132022.136426.
(45) Liu, H.; Cheng, M.; Liu, Y.; Zhang, G.; Li, L.; Du, L.; Li, B.; Xiao, S.; Wang, G.; Yang, X. Modified UiO-66 as photocatalysts for boosting the carbon-neutral energy cycle and solving environmental remediation issues. *Coord. Chem. Rev.* **2022**, *458*, 214428. https://doi.org/214410.211016/j.ccr.212022.214428.
(46) Duflot, M.; Marchal, C.; Caps, V.; Artero, V.; Christoforidis, K.; Keller, V. Optimization of NH2-UiO-66/TiO2/Au composites for enhanced gas-phase CO2 photocatalytic reduction into CH4. *Catal. Today* **2023**, *413-415*, 114018.
(47) Melillo, A. G.-A., R.; Navalon, S.; Atienzar, P.; Ferrer, B.; Álvaro, M.; Garcia, H. Photoactive Zr and Ti metal-organic-frameworks for solid-state solar cells. *ChemPhysChem* **2021**, *22*, 842-848. https://doi.org/810.1002/cphc.202100083.
(48) Santiago-Portillo, A.; Baldoví, H. G.; Fernandez, M. T. G.; Navalón, S.; Atienzar, P.; Ferrer, B.; Alvaro, M.; Garcia, H.; Li, Z. Ti as mediator in the photoinduced electron transfer of mixed-metal NH2–UiO-66(Zr/Ti): transient absorption spectroscopy study and application in photovoltaic cell. *J. Phys. Chem. C* **2017**, *121*, 7015-7024. https://doi.org/7010.1021/acs.jpcc.7016b13068.
(49) Rada, Z. H.; Abid, H. R.; Sun, H.; Shang, J.; Li, J.; He, Y.; Liu, S.; Wang, S. Effects of -NO2 and -NH2 functional groups in mixed-linker Zr-based MOFs on gas adsorption of CO2 and CH4. *Prog. Nat. Sci.: Mater. Int.* **2018**, *28*, 160-167.
(50) Rueda-Navarro, C. M. F., B.; Baldoví, H.G.; Navalón, S. Photocatalytic hydrogen production from glycerol aqueous solutions as sustainable feedstocks using Zr-based UiO-66 materials under simulated sunlight irradiation. *Nanomaterials* **2022**, *12*, 3808. https://doi.org/3810.3390/nano12213808.
(51) Dai, S. M.-L., E.; Tissot, A.; Baldoví, H. G.; García, H.; Navalón, S.; Serre, C. . Room temperature design of Ce(IV)-MOFs: from photocatalytic HER and OER to overall water splitting under simulated sunlight irradiation. *Chem. Sci.* **2023**, *14*, 3451–3461. https://doi.org/3410.1039/D3452SC05161C.

(52) Cabrero-Antonino, M. M., A.; Montero-Lanzuela, E.; Álvaro, M.; Ferrer, B.; Vayá, I.; Baldoví, H.G.; Navalón, S. Solar-driven gas phase photocatalytic CO2 methanation by multimetallic UiO-66 solids decorated with RuOx nanoparticles. *Chem. Eng. J.* **2023**, *468*, 143553.
(53) Wu, X.-P.; Gagliardi, L.; Truhlar, D. G. Metal doping in cerium metal-organic frameworks for visible-response water splitting photocatalysts. *J. Chem. Phys.* **2019**, *150*, 041701.
(54) Wu, X.-P.; Gagliardi, L.; Truhlar, D. G. Metal doping in cerium metal-organic frameworks for visible-response water splitting photocatalysts. *J. Chem. Phys.* **2019**, *150*, 041701. https://doi.org/041710.041063/041701.5043538.
(55) Rueda-Navarro, C. M., ; ; Cabrero-Antonino, M.; Escamilla, P.; Díez-Cabanes, V.; Fan, D.; Atienzar, P.; Ferrer B.; Vayá, I.; Maurin, G.; Baldoví, H. G.; et al. Solar-assisted photocatalytic water splitting using defective UiO-66 solids from modulated synthesis. *Nano Res.* **2023**, https://doi.org/10.1007/s12274-12023-16351-12271.
(56) Shearer, G. C.; Chavan, S.; Bordiga, S.; Svelle, S.; Olsbye, U.; Lillerud, K. P. Defect engineering: tuning the porosity and composition of the metal−organic framework UiO-66 via modulated synthesis. *Chem. Mater.* **2016**, *28*, 3749−3761. https://doi.org/3710.1021/acs.chemmater.3746b00602.
(57) Cavka, J. H.; Jakobsen, S.; Olsbye, U.; Guillou, N.; Lamberti, C.; Bordiga, S.; Lillerud, K. A new zirconium inorganic building brick forming metal organic frameworks with exceptional stability. . *J. Am. Chem. Soc.* **2008**, *130*, 13850-13851. https://doi.org/13810.11021/ja8057953.
(58) Santiago-Portillo, A.; Navalón, S.; lvaro, M.; García, H. Generating and optimizing the catalytic activity in UiO-66 for aerobic oxidation of alkenes by post-synthetic exchange Ti atoms combined with ligand substitution. *J. Catal.* **2018**, *365*, 450-463.
(59) Sun, D.; Liu, W.; Qiu, M.; Zhang, Y.; Li, Z. Introduction of a mediator for enhancing photocatalytic performance via post-synthetic metal exchange in metal–organic frameworks (MOFs). *Chem. Commun.* **2015**, *51*, 2056-2059.
(60) Santaclara, J. G.; Olivos-Suarez, A. I.; Gonzalez-Nelson, A.; Osadchii, D.; Nasalevich, M. A.; van der Veen, M. A.; Kapteijn, F.; Sheveleva, A. M.; Veber, S. L.; Fedin, M. V.; et al. Revisiting the Incorporation of Ti(IV) in UiO-type Metal–Organic Frameworks: Metal Exchange versus Grafting and Their Implications on Photocatalysis. *Chem. Mater.* **2017**, *29*, 8963-8967.
(61) Wang, Y. L., H.; Zhou, W.; Zhang, X.; Zhang, B.; Yu, Y. Structurally disordered RuO2 nanosheets with rich oxygen vacancies for enhanced nitrate electroreduction to ammonia. *Angew. Chem. Int. Ed.* **2022**, *61*, e202202604.
(62) Rueda-Navarro, C. M.; Ferrer, B.; Baldoví, H. G.; Navalon, S. Photocatalytic hydrogen production from glycerol aqueous solutions as sustainable feedstocks using Zr-based UiO-66 materials under simulated sunlight irradiation. *Nanomaterials* **2022**, *12*, 3808. https://doi.org/3810.3390/nano12213808.
(63) Kandiah, M. N., M.H.; Usseglio, S.; Jakobsen, S.; Olsbye, U.; Tilset, M.; Larabi, C.; Quadrelli, E.A.; Bonino, F.; Lillerud, K.P. Synthesis and stability of tagged UiO-66 Zr-MOFs. *Chem. Mater.* **2010**, *22*, 6632-6640.
(64) Zhu, J. W., L.; Bu, Z.; Jie, S.; Li, B.-G. Polyethyleneimine-modified UiO-66-NH2(Zr) metal–organic frameworks: preparation and enhanced CO2 selective adsorption. *ACS Omega* **2019**, *4*, 3188–3197.
(65) Nasalevich, M. A.; Van Der Veen, M.; Kapteijn, F.; Gascon, J. Metal-organic frameworks as heterogeneous photocatalysts: Advantages and challenges. *CrystEngComm* **2014**, *16*, 4919-4926.
(66) Hendrickx, K.; Vanpoucke, D. E. P.; Leus, K.; Lejaeghere, K.; Van Yperen-De Deyne, A. V.; Van Speybroeck, V.; Van Der Voort, P.; Hemelsoet, K. Understanding intrinsic light absorption properties of UiO-66 frameworks: A combined theoretical and experimental

study. *Inorg. Chem.* **2015**, *54*, 10701-10710. https://doi.org/10710.11021/acs.inorgchem.10705b01593.
(67) Wu, X.-P.; Gagliardi, L.; Truhlar, D. G. Cerium metal–organic framework for photocatalysis. *J. Am. Chem. Soc.* **2018**, *140*, 7904-7912. https://doi.org/7910.1021/jacs.7908b03613.
(68) Zhang, J. C., H.; Duan, X.; Sun, H.; Wang, S. Photothermal catalysis: from fundamentals to practical applications. *Mater. Today* **2023**, *268*, 234-253.
(69) Zhang, X. L., X.; Zhang, D.; Su, N.Q.; Yang, W.; Everitt, H.O.; Liu, J. Product selectivity in plasmonic photocatalysis for carbon dioxide hydrogenation. *Nat. Commun.* **2018**, *8*, 14542.
(70) Luo, S. L., H.; Wang, Q.; Ren, X.; Hernández-Pinilla, D.; Nagao, R.; Xie, Y.; Yang, G.; Li, S.; Song, H.; Oshikiri, M.; Ye, J. Triggering water and methanol activation for solar-driven H2 production: Interplay of dual active sites over plasmonic ZnCu alloy. *J. Am. Chem. Soc.* **2021**, *143*, 12145−12153.
(71) Ren, J. O., S.; Xu, H.; Meng, X.; Wang, T.; Wang, D.; Ye, J. Targeting activation of CO2 and H2 over Ru-loaded ultrathin layered double hydroxides to achieve efficient photothermal CO2 methanation in flow-type system. *Adv. Energy Mater.* **2016**, 1601657.
(72) Guo, C. T., Y.; Yang, Z.; Zhao, T.; Liu, J.; Zhao, Y.; Wang, F. Reinforcing the efficiency of photothermal catalytic CO2 methanation through integration of Ru nanoparticles with photothermal MnCo2O4 nanosheets. *ACS Nano* **2023**, *17*, 23761−23771.
(73) Xiong, K. W., Y.; Zhang, F.; Li, X.; Lang, X. Linker length-dependent photocatalytic activity of β-ketoenamine covalent organic frameworks. *Appl. Catal. B.-Environ* **2023**, *322*, 122135.
(74) Yan, X. C., M.; Li, S.; Duchesne, P.N.; Sun, W.; Mao, C.; Song, R.; Lu, Z.; Chen, X.; Qian, W.; Li, R.; Wang, L.; Ozin, G.A. Visualizing the birth and monitoring the life of a bimetallic methanation catalyst. *J. Am. Chem. Soc.* **2023**, *145*, 27358−27366.
(75) Beuls, A. S., C.; Jacquemin, M.; Heyen, G.; Karelovic, A.; Ruiz, P. CO2 hydrogenation at low temperature over Rh/γ-Al2O3 catalysts: Effect of the metal particle size on catalytic performances and reaction mechanism. *Appl. Catal. B* **2012**, *113–114*, 237-249.
(76) Mateo, D.; Santiago-Portillo, A.; Albero, J.; Navalón, S.; Alvaro, M.; García, H. Long-term photostability in Terephthalate Metal Organic Frameworks. *Angew. Chem. Int. Ed.* **2019**, *58*, 17843-17848.
(77) Mateo, D. C., J.L.; Durini, S.; Gascon, J. Fundamentals and applications of photo-thermal catalysis. *Chem. Soc. Rev.* **2021**, *50*, 2173-2210. https://doi.org/2110.1039/D2170CS00357C.
(78) Khan, I. S. G.-T., L.; Mateo, D.; Gascon, J. Metal-organic-frameworks and their derived materials in photo-thermal catalysis. *Eur. J. Inorg. Chem.* **2022**, *28*, e202200316.
(79) Song, C. W., Z.; Yin, Z.; Xiao, D.; Ma, D. Principles and applications of photothermal catalysis. *Chem Catal,* **2022**, *2*, 52–83.
(80) Ruckebusch, C. S., M.; Pernot, P.; de Juan, A.; Tauler, R. Comprehensive data analysis of femtosecond transient absorption spectra: A review. *J. Photochem. Photobiol. C* **2012**, *13*, 1-27.
(81) Ma, X.; Wang, L.; Zhang, Q.; Jiang, H.-L. Switching on the photocatalysis of metal–organic frameworks by engineering structural defects. *Angew. Chem. Int. Ed.* **2019**, *58*, 12175 –12179. https://doi.org/12110.11002/anie.201907074.
(82) Xiao, J.-D.; Shang, Q.; Xiong, Y.; Zhang, Q.; Luo, Y.; Yu, S.-H.; Jiang, H.-L. Boosting photocatalytic hydrogen production of a metal–organic framework decorated with platinum nanoparticles: The platinum location matters. *Angew. Chem. Int. Ed.* **2016**, *128*, 9535-9539.
(83) Cabrero-Antonino, M.; Melillo, A.; Montero-Lanzuela, E.; Álvaro, M.; Ferrer, B.; Vayá, I.; Baldoví, H. G.; Navalón, S. Solar-driven gas phase photocatalytic CO2 methanation by

multimetallic UiO-66 solids decorated with RuOx nanoparticles. *Chem. Eng. J.* **2023**, *468*. DOI: 10.1016/j.cej.2023.143553.
(84) Melillo, A.; Cabrero-Antonino, M.; Navalón, S.; Álvaro, M.; Ferrer, B.; García, H. Enhancing visible-light photocatalytic activity for overall water splitting in UiO-66 by controlling metal node composition. *Appl. Catal. B* **2020**, *278*. DOI: 10.1016/j.apcatb.2020.119345.
(85) Bhattacharyy, A. G., M.; Cohen, B.; Szalad, H.; Albero, J.; Garcia, H.; Douhal, A. Unraveling the optimal cerium content for boosting the photoresponse activity of mixed-metal Zr/Ce-based metal–organic frameworks through a photodynamic and photocurrent correlation: Implications on water splitting efficiency. *ACS Appl. Mater. Interfaces* **2023**, *15*, 36434–36446. https://doi.org/36410.31021/acsami.36433c08062.
(86) Bhattacharyya, A.; Gutiérrez, M.; Cohen, B.; Valverde-González, A.; Iglesias, M.; Douhal, A. How does the metal doping in mixed metal MOFs influence their photodynamics? A direct evidence for improved photocatalysts. *Mater. Today Energy* **2022**, *29*, 101125. https://doi.org/101110.101016/j.mtener.102022.101125.
(87) Yu, X. M. L., J.; Du, M. H.; Song, X. J.; Huang, H. L.; Nie, L. Adaptive lattice-matched MOF and COF core–shell heterostructure for carbon dioxide photoreduction. *Cell Rep. Phys. Sci.* **2023**, *4*, 101657.
(88) Mascaretti L.; Schirato, A. M., T.; Alabastri, A.; Naldoni, A.; Fornasiero, P. Challenges in temperature measurements in gas-phase photothermal catalysis. *Joule* **2022**, *6*, 1727–1742.
(89) Liu, L.; Zhong, K.; Meng, L.; Hemelrijck, D. V.; Wang, L.; Glorieux, C. Temperature-sensitive photoluminescent CdSe-ZnS polymer composite film for lock-in photothermal characterization. *J. Appl. Phys.* **2016**, *119*, 224902
(90) Su, B. K., Y.; Wang, S.; Zuo, S.; Lin, W.; Fang, Y.; Hou, Y.; Zhang, G.; Zhang, H.; Wang, X. Hydroxyl-bonded Ru on metallic TiN surface catalyzing CO2 reduction with H2O by infrared light. *J. Am. Chem. Soc.* **2023**, *145*, 27415–27423.
(91) Wang, Y. L., Y.; Tan, L.; Lin, X.; Fang, Y.; Lu, X.F.; Hou, Y.; Zhang, G.; Wang, S. Confining ultrafine Pt nanoparticles on In2O3 nanotubes for enhanced selective methanol production by CO2 hydrogenation. *J. Mater. Chem. A* **2023**, *11*, 26804–26811.
(92) Kattel, S. L., P.; Chen, J.G. Tuning selectivity of CO2 hydrogenation reactions at the metal/oxide interface. *J. Am. Chem. Soc.* **2017**, *139*, 9739–9754.